Identification of a novel and ancestral machinery involved in mitochondrial membrane branching in *Trypanosoma brucei*

Short title: Mitochondrial dynamics in trypanosomes

Chloé Alexandra Morel[1], Corinne Asencio[1], Corinne Blancard[2], Bénédicte Salin[2], Etienne Gontier[3], Stéphane Duvezin-Caubet[2], Manuel Rojo[2], Frédéric Bringaud[1] and Emmanuel Tetaud[1*]

[1] Univ. Bordeaux, CNRS, MFP, UMR 5234, F-33000, Bordeaux, France

[2] Univ. Bordeaux, CNRS, IBGC, UMR 5095, F-33000, Bordeaux, France

[3] Univ. Bordeaux, BIC, F-33000, Bordeaux, France

*Corresponding author: emmanuel.tetaud@u-bordeaux.fr

Tel: (+33) 0557574805

ABSTRACT

African trypanosomes are eukaryotic parasites that exist in two main replicative forms; the procyclic form in the midgut of the insect vector, the tsetse fly Glossina spp. and the bloodstream form responsible for diseases in humans and cattle. Unlike most other eukaryotes, where mitochondria continuously fuse and divide, trypanosome mitochondria form a single and continuously interconnected network that only divides during cytokinesis. The machineries governing mitochondrial remodeling and interconnection, however, remain largely unknown. We characterize a dynamin-related protein (DRP) from *T. brucei* (*Tb*DBF, previously called *Tb*MfnL) that depicts sequence similarities with Opa1 and Mfn, mammalian DRPs involved mitochondrial fusion. We showed that *Tb*DBF has closely related homologues in several organisms that are devoid of Mfn and Opa1, such as eukaryotes from different phyla, prokaryotes and archaea. *Tb*DBF is the first member of this new protein family to be functionally characterized. It localizes to the mitochondrial periphery and, upon overexpression, induces a strong increase in the interconnection and branching of mitochondrial filaments in a GTPase dependent manner. Its overexpression also promotes a major increase in cellular and mitochondrial volume and an increased consumption of the two major carbon sources used by the parasite (glucose and proline), as well as ethanolamine, a precursor of phosphatidyl-ethanolamine involved in membrane biogenesis and shaping. We propose that mitochondrial *Tb*DBF is a component of an ancestral membrane remodeling machinery that contributes to the formation of intermitochondrial connections.

37 ***INTRODUCTION***

38 *Trypanosoma brucei* is a parasite responsible for African sleeping sickness as well
39 as the related cattle disease Nagana, affecting sub-Saharan Africa. *T. brucei* is
40 transmitted to mammals, its final host, by an insect vector: the tsetse fly. During the
41 trypanosome life cycle, the parasite exists in at least two replicative forms; the procyclic
42 form (PCF), transmitted by the tsetse fly Glossina spp., and the bloodstream form (BSF)
43 responsible for diseases in vertebrates. The pathogenic trypanosomes have a single
44 mitochondrion, unlike most other eukaryotes that contain numerous ones (1).
45 Trypanosome's mitochondrion is highly elongated and reticulated and its genome
46 (mitochondrial DNA) is restricted to a specific structure at the basis of the flagellum
47 known as kinetoplast (kDNA). During the trypanosome life cycle and its adaptation to
48 different hosts and environments, the shape of its mitochondrial compartment undergoes
49 spectacular changes that reflect its functional plasticity. Indeed, the mitochondrion of this
50 parasite exists in at least two major forms: (i) the fully active and developed one
51 characteristic for the PCF that harbors the oxidative phosphorylation complexes
52 (OXPHOS) for energy production (2, 3) and (ii) the functionally less active and
53 morphologically reduced form found in the bloodstream, with energy produced
54 exclusively through glycolysis since OXPHOS is repressed (4). These modifications
55 correlate with the adaptation of the parasite to the glucose-rich blood of a mammalian
56 host and the proline-rich hemolymph and tissue fluids of the blood-feeding tsetse fly (5).
57 Studies in mammals and in yeast having unraveled tight links between mitochondrial
58 bioenergetics, morphology and dynamics (6-8), it is tempting to assume that such close
59 relationships not only regulate mitochondrial function and energy metabolism, but also
60 the life cycle and pathogenic potential of trypanosomes. However, in contrast to fungi
61 and metazoa, where mitochondrial morphology and fusion/fission dynamics have been
62 thoroughly characterized (9, 10), little is known about the morphology and dynamics of
63 mitochondria in trypanosomes.

64 In most eukaryotes, mitochondria are very dynamic, alternating between two major
65 events; fusion and fission. Mitochondrial dynamics allows to maintain mitochondrial

66 morphology, distribution and size (7). The main proteins involved in these events are
67 large GTPase belonging to the dynamin family. The main GTPase responsible for
68 mitochondrial fission in yeast and mammalian cells is Dnm1/Drp1, a soluble protein
69 which is recruited to mitochondrial and peroxisomal membranes to exert its function (11,
70 12). Mammalian mitochondrial fusion requires fusion of outer mitochondrial membrane
71 (OMM) followed by fusion of inner mitochondrial membrane (IMM) which is carried out by
72 mitofusins 1 and 2 (Mfn1 and Mfn2) and optic atrophy 1 (Opa1), respectively (13, 14).
73 Alteration in one of these processes and of the equilibrium between them provokes
74 mitochondrial fragmentation or hyperfusion (11, 15) and is linked to diseases, notably
75 neuropathies (16).

76 Mitochondrial fusion and fission in trypanosomes have been poorly investigated to
77 date. Unlike mammalian and yeast cells, fusion has not been directly observed (17, 18),
78 but indirect evidence for mitochondrial fusion came 25 years ago from *in vivo* genetic
79 exchange of mtDNA (19). Another indication of fusion stems from the observation that
80 the mitochondrial fragmentation provoked by the overexpression of mammalian Bax in
81 trypanosomes is reversible (20) and from the observation that, in BSF, the mitochondrial
82 network mostly grows from two areas where loops and branches eventually merge to
83 build a complex network (17). Available evidence indicates that mitochondrial fission is
84 not an endogenous/spontaneous process (17, 18) but it has to be artificially induced to
85 be observed (20, 21) and appears restricted to parasite division (18, 21). More recently,
86 expression, in the mitochondrial matrix of trypanosome, of a putative dynamin from
87 giant viruses has shown remodeling of the mitochondrion into a simple tubular structure,
88 supporting that mitochondrial fission occurs in this parasite (22). The absence of
89 spontaneous, ongoing or continuous fission could explain the unique tubular and
90 reticulated structure of the parasite mitochondrion, resembling that observed in yeast or
91 mammalian mutants devoid of fission (23, 24). Finally, a recent study of the
92 mitochondrial structure in another trypanosomatid (*Crithidia fasciculata*), revealed slow
93 and discrete fission and fusion events during the cell cycle, suggesting that fusion/fission
94 machineries must exist in trypanosomatids (25).

95 Two decades of research have revealed that numerous mitochondrial fusion and
96 fission factors appear conserved in fungi and mammals with non-neglectable differences
97 (7). In plants, mitochondria fuse and divide, but factors directly involved in fusion have
98 not been clearly identified until now, suggesting the existence of a different fusion
99 machineries (26, 27). So far, only one dynamin-related protein (DRP), *Tb*Dlp, has been
100 described and studied in *T. brucei*: its ablation impairs mitochondrial division and
101 endocytosis and leads to cytokinesis arrest (21, 28). *Tb*Dlp thus appears to be the
102 functional homolog of Drp1/Dnm1 in mammals and yeast, but its fission activity seems
103 restricted to the cytokinesis (21). Another putative DRP displaying some similarity to
104 mitofusins (*Tb*MFNL, Tb927.7.2410) has been reported to influence the mitochondrial
105 shape (29). Its down-regulation led to a highly fenestrated mitochondrial network,
106 suggesting that, despite its name, it plays a role in mitochondrial fission (29). To date,
107 no protein has been involved in mitochondrial fusion in trypanosomes.
108 In this study, we characterized the trypanosome DRP named *Tb*MFNL (29). We
109 show that this DRP shows a strong similarity with a family of eukaryotic, prokaryotic and
110 archaeal proteins that is absent from all organisms expressing Mfn or Opa1 homologues
111 (fungi and mammals) and from plants, suggesting that it belongs to an ancestral
112 membrane remodeling machinery. We show that it localizes to mitochondrial membranes
113 and is able to modulate mitochondrial branching and shape. Its deletion does not alter
114 mitochondrial morphology or distribution but its overexpression increases the size and
115 branching of its mitochondrial compartment in a GTP-dependent manner. Taken
116 together, our findings reveal that mitochondrial branching in trypanosomes is modulated
117 by a member of a novel and ancestral membrane remodeling machinery that we have
118 named *Tb*DBF for *Trypanosoma brucei* Dynamin-related Branching Factor.

119 ## *RESULTS*

120 ### *1 - Identification and sequence analysis of TbDBF*

121 To identify potential fusion players, we started our search by careful re-examination
122 of trypanosome genomic and proteomic databases for proteins showing sequence
123 homology to known fusion factors (Opa1/Mfn1/2). We were only able to identify the
124 previously reported dynamin-related protein *Tb*MFNL (Tb927.7.2410) (29), that displays
125 some similarities with both mammalian fusion factors of the inner (Opa1) or outer
126 membrane (Mfn2) with 21 and 23 % of sequence identity, respectively (**Figure 1, S1**
127 **and Table S1**). Analysis of its sequence identified several motifs and domains found in
128 other mitochondrial DRPs. Indeed, its N-terminal sequence displays a potential
129 mitochondrial targeting signal (MTS) with potential cleavage sites (**Figure S1**), followed
130 by a GTPase domain with conserved G1 to G4 motifs and, in its C-terminal region, two
131 consecutive transmembrane domains (TM) (**Figure 1 and S1**). Interestingly, the MTS
132 points to inner membrane targeting (such as the inner membrane fusion factor Opa1
133 localizing to the intermembrane space). In contrast to Opa1, that carries an N-proximal
134 TM domain mediating inner membrane anchoring, no transmembrane domain was
135 identified following the MTS, suggesting that it is not an Opa1 counterpart. The overall
136 structure and domain organization of the protein displays more similarity to human Mfn
137 (**Figure 1**) with two C-proximal transmembrane domains (TMs) that are reminiscent of
138 the targeting to the outer mitochondrial membrane of Mfn. However, the presence of a
139 N-terminal MTS makes it unlikely to be located in the outer membrane like Mfn in
140 mammals. Altogether, these data suggest that the protein named *Tb*MFNL (29) is not a
141 homolog of fusion factors Opa1 or Mfn.

142 We therefore investigated whether this DRP could be conserved in other organisms.
143 As expected, it is well conserved throughout the *kinetoplastida* order (**Figure S2 and**
144 **Table S1** for some examples) but, surprisingly, we identify homologous proteins, with
145 high similarity over the whole sequence, in many eukaryote lineages (mainly in the SAR
146 clade *Stramenopiles* and *Alveolata*) (**Figure 2A, S3 and Table S1**) but never in
147 *Opisthokonta* (clade including fungi and mammals) or in plants. Unexpectedly, we also

148 identified many similar sequences in bacteria, mainly in the PVC group and in
149 proteobacteria (**Figure 2A**). Finally, a sequence was also identified in *Archaea*, revealing
150 that, unlike Opa1 and Mfn proteins, the proteins of this family are conserved in all the
151 three domains of life (**Figure 2A, S3 and Table S1**). Remarkably, we could not identify
152 sequences corresponding to Opa1 and Mfn in any of these organisms, the only sequences
153 identified being restricted, as anticipated, to the well-conserved GTPase domain.
154 Phylogenetic analysis was carried out using the amino acid sequences of the proteins and
155 a comprehensive tree based on sequence alignment is shown in **Figure 2B**. Structural
156 analysis of several of these identified proteins, show again a very conserved structural
157 organization on the whole sequence (**Figure 2C and S3**). Indeed, apart from the
158 obvious absence of the MTS in prokaryotes, the general structure and domain
159 organization are extremely well preserved (**Figure 2C**). Altogether, our analysis shows
160 that these proteins form a phylogenetic group that is clearly separated from the well-
161 known fusion and fission dynamins of fungi and mammals and of *Np*BDLP, its closest
162 bacterial homologue (**Figure 2B**). As these DRPs are conserved throughout the living
163 world, but not in fungi, mammals, and plants, it is tempting to speculate that they
164 represent a component of a novel and ancestral machinery involved in membrane
165 dynamics. Their belonging to a protein family different from that of mitofusins and the
166 functional characterization described below led us to rename this DRP *Tb*DBF (for
167 *Trypanosoma brucei* Dynamin-related Branching Factor).
168
169 ***2 - TbDBF is localized in the mitochondrion***
170 Interrogation of the TrypTag database (cellular localization of trypanosome proteins
171 (30)) with the *Tb*DBF sequence (Tb927.07.2410) reveals mitochondrial localization for a
172 C-terminal GFP-tagged version and a cytoplasmic, flagellar and nuclear lumen
173 localization for an N-terminal GFP tagged construct. One potential explanation for this
174 apparent discrepancy is that adding an N-terminal GFP sequence in front of a
175 mitochondrial targeting sequence (MTS) is expected to perturb its addressing and
176 therefore does not allow to conclude on its localization. To confirm the subcellular

177 localization of *Tb*DBF in *T. brucei*, we added a C-terminal 10xHA tag (to avoid disruption
178 of mitochondrial targeting) to endogenous *Tb*DBF (*Tb*DBF$_{::10HA}$) in both PCF and BSF
179 using the pPOTV7 vector series (31) (**Figure 3A**) and verified that the tag has no impact
180 on cell growth (**Figure S4**). It should be noted that the slight variation in growth
181 observed between the wild-type and the tagged strain could be due to the difference
182 between a non-clonal (wild-type) and clonal (*Tb*DBF$_{::10HA}$) population. Expression of
183 *Tb*DBF$_{::10HA}$ was confirmed by western-blot with anti-HA antibody in PCF and BSF (**Figure**
184 **3B**). The protein is about 2-fold more expressed in PCF than BSF which is in agreement
185 with the data obtained by SILAC analysis for this protein (32). The localization of the
186 *Tb*DBF protein was studied in PCF by immunofluorescence using threonine
187 dehydrogenase (Tdh, (33)) as a mitochondrial matrix marker (**Figure 3C**). *Tb*DBF$_{::10HA}$
188 and Tdh clearly colocalized in the mitochondrial compartment, but *Tb*DBF depicted a less
189 homogeneous mitochondrial distribution (**Figure 3C, Anti-HA/Merge**). We also
190 addressed, by immunofluorescence*, Tb*DBF subcellular localization in BSF. For technical
191 reasons (Tdh antibody do not react in bloodstream and the lack of primary antibody of
192 non-murine origin), we could not perform a colocalization of the *Tb*DBF$_{::10HA}$ protein with
193 a mitochondrial protein. However, we performed a parallel labeling of the mitochondria,
194 with an antibody directed against the mitochondrial Hsp60 or against the HA-tag. Under
195 these conditions, we observe a tubular structure characteristic of the BSF mitochondrion
196 both for *Tb*DBF and Hsp60 (**Figure 3D**). The overall modular organization of *Tb*DBF
197 previously described and its subcellular localization confirm that *Tb*DBF is a mitochondrial
198 protein.
199
200 ***3 – Inactivation and silencing of TbDBF does not alter mitochondrial shape***
201 Live microscopy of yeasts and cultured mammalian cells has revealed that
202 mitochondrial morphology is continuously remodeled by antagonizing fission and fusion
203 reactions (15, 34). Under normal conditions, the fusion/fission balance is established in
204 favor of fusion and the mitochondria appear filamentous. Inhibition of fusion leads to
205 mitochondrial fragmentation by ongoing fission (15) and reversely enhancing fusion leads

206 to hyperfused mitochondria with increased branching and interconnection (11). In
207 contrast, trypanosomes show a single permanently branched and interconnected
208 mitochondrion, with very few mitochondrial fission events reported, which appear to be
209 restricted to cell division and especially cytokinesis (18, 21).

210 To investigate the role of *Tb*DBF, we first inactivated the gene encoding *Tb*DBF by
211 CRISPR/Cas9 (35) with an optimized protocol (see Materials and Methods). Both *Tb*DBF
212 alleles were inactivated by integration of a puromycin resistance marker cassette into
213 both PCF and BSF cells (**Figure 4A**). Cloned parasites were analyzed by PCR to select
214 cell lines carrying PAC insertions in both *Tb*DBF alleles (*Tb*DBF$^{-/-}$) (**Figure 4B**). No
215 significant impact on cell growth was observed in these PCF and BSF null-mutants over a
216 period of 7 days compared to wild-type cells. We infer that the slight variation in growth
217 observed between the wild-type and the inactivated strain reflects the difference
218 between a non-clonal (wild-type) and clonal (*Tb*DBF$^{-/-}$) population (**Figure S4**). To
219 investigate potential impact of *Tb*DBF$^{-/-}$ on mitochondrial shape, we labeled PCF
220 mitochondria with rhodamine-123 staining and analyzed mitochondrial shape in living
221 cells. Since BSF were too mobile to obtain focused images with rhodamine 123, we
222 stained mitochondria in fixed cells by immunofluorescence with mitochondrial Hsp60
223 antibodies. In both PCF and BSF, no significant difference in the structure of the *Tb*DBF$^{-/-}$
224 mitochondrion was observed (**Figure 4C and 4E**). To confirm that this strategy leads to
225 *Tb*BDF inactivation, we repeated this process in a strain endotagged with a C-terminal
226 3xTy1 tag in order to follow the expression of the protein by western-blot (**Figure S5/A-**
227 **D**). Two separate inactivations were performed, one by inserting the puromycin
228 resistance gene as before (**Figure S5E-G**) and the other one by deleting part of the gene
229 (**Figure S5H-J**). In both cases, the protein was not detected in the inactivated clones
230 and no modification of the mitochondrial structure was observed (**Figure S5G/J)**.

231 In order to detect and quantify discrete modifications of the mitochondrial shape
232 that may escape detection upon qualitative visual analysis, we developed an ImageJ
233 macro (**Supplemental MMS1**) for the automatic analysis of the obtained images, which
234 allows quantification of mitochondrial junctions (**Figure 4D**). This allowed us to establish

235 that the number of mitochondrial junctions is equivalent in *Tb*DBF$^{-/-}$ and wild-type PCF
236 cells (8.5±4.9 vs 9.4±4.3) confirming the qualitative analysis of the microscopy images
237 (**Figure 4C**). These findings regarding the consequences of *Tb*DBF inactivation in PCF
238 and BSF are not in line with a previous report describing a highly fenestrated
239 mitochondrial network consecutive to a partial but significant inhibition (70%) of *Tb*DBF
240 (*Tb*MFNL) expression by RNAi in BSF (29). To exclude that the divergence arose from the
241 different inactivation and silencing strategies, we conditionally down-regulated
242 expression of *Tb*DBF using a stem-loop RNAi construct. This approach led to a significant
243 reduction (~70%) of the expression of endogenously tagged *Tb*DBF$_{::10HA}$ in PCF (as
244 observed in BSF (29)), but this was not paralleled by a modification of mitochondrial
245 shape (**Figure S6A-C**). Since mitochondrial fenestration upon *Tb*MFNL/*Tb*DBF silencing
246 was observed in BSF (29) we decided to repeat the experiment using the same strain (*T.*
247 *brucei* 427 BSF), the same RNAi system (p2T7-177) and the same sequence used for
248 down-regulation (29). As previously reported (29), we observed a significant reduction of
249 *T*bDBF expression (~80% after 4 days) of the endogenously tagged *Tb*DBF$_{::3HA}$ in BSF
250 (**Figure S6D-F**) that was not accompanied by mitochondrial shape modifications (**Figure**
251 **S6G**). In our hands, neither inactivation nor silencing of *Tb*MFNL/*Tb*DBF alters
252 mitochondrial morphology or induces a fenestration phenotype. At present, we ignore the
253 reasons for the discrepancy with the results reported by Vanwalleghem et *al*. (29).
254

255 ***4 - TbDBF overexpression increases mitochondrial branching in a GTP-***
256 ***dependant manner***

257 We also investigated the possible role of *Tb*DBF by conditionally expressing a C-
258 terminally-tagged (3xTy1) *Tb*DBF (^{oe}*Tb*DBF$_{::3Ty1}$) in PCF (**Figure 5A**). Expression was
259 confirmed by western-blot analysis after 3 to 5 days of tetracycline induction (**Figure**
260 **5B**). Rhodamine-123 staining showed that wild-type and non-induced ^{oe}*Tb*DBF$_{::3Ty1}$ cells
261 harbor the expected reticulated mitochondrial structure, while the mitochondrion appears
262 significantly more reticulated and branched in induced ^{oe}*Tb*DBF$_{::3Ty1}$ cells (**Figure 5C and**
263 **Figure S7**). For a more precise and quantitative description of the branching phenotype,

264 we used our ImageJ macro allowing quantification of mitochondrial junctions. After 5
265 days of induction, the average number of mitochondrial junctions appeared more than 2-
266 times higher in induced ^{oe}*Tb*DBF$_{::3Ty1}$ cells compared to non-induced or wild type cells
267 (**Figure 5G**). In order to estimate the level of *Tb*DBF overexpression achieved in *T.*
268 *brucei* PCF, we repeated this experiment with cells expressing endogenously 3Ty1-tagged
269 *Tb*DBF (*Tb*DBF$_{::3Ty1}$, clone 2A11; **Figure S5A-D**). Western-blot analysis revealed that
270 upon induction, exogenous *Tb*DBF$_{::3Ty1}$ protein is well overexpressed relative to its
271 endogenous expression and induces alterations of mitochondrial shape (**Figure S8A/B**).
272 It is also noteworthy that the expression of *Tb*DBF without the C-terminal 3Ty1 tag
273 induces the same phenotype as the tagged *Tb*DBF, confirming that the phenotype is not
274 due to the use of a C-terminal tag (**Figure S8A/B**). These data clearly demonstrate that
275 overexpression of *Tb*DBF stimulates intermitochondrial connections.
276 All Dynamin-like proteins possess a GTP-binding domain that binds and hydrolyzes
277 GTP and mutations in the highly conserved domains interacting with GTP provoke
278 dynamin-dysfunction by lowering GTP-binding and hydrolysis efficiency. To determine
279 whether *Tb*DBF requires a functional GTPase domain to function, the key lysine 141 in
280 the highly conserved G1 motif was converted to alanine, a mutation (K141A) significantly
281 reducing GTP-binding of dynamins in other organisms (36-38). The K141A mutation was
282 introduced into the sequence of *Tb*DBF tagged with a C-terminal 3Ty1
283 (^{oe}*Tb*DBFK141A$_{::3Ty1}$, **Figure 5D**). Expression was confirmed by western-blot analysis
284 after 3 to 5 days of tetracycline induction (**Figure 5E**) and overexpression of
285 *Tb*DBFK141A$_{::3Ty1}$ was also confirmed as the wild-type *Tb*DBF$_{::3Ty1}$ (**Figure S8A**). The
286 mutated protein localized to the mitochondria (**Figure 6D**), as expected, but did not alter
287 mitochondrial shape (**Figure 5F, Figure S7**) nor the number of mitochondrial junctions
288 (**Figure 5G**). This clearly demonstrates that *Tb*DBF is a dynamin related protein that
289 relies on a functional GTPase domain to modulate mitochondrial branching in
290 trypanosomes.
291
292 ***5 - Submitochondrial localization of TbDBF***

293 The localization of overexpressed *Tb*DBF was also analyzed by immunofluorescence.
294 The overexpressed *Tb*DBF$_{::3Ty1}$ co-localized with Tdh in mitochondria (**Figure 6A-d5.i**),
295 as previously described for the endogenous protein (**Figure 3C**). Analysis of
296 mitochondrial shape by immunofluorescence confirmed that overexpression of *Tb*DBF is
297 linked to the appearance of hyper-reticulated mitochondrion (**Figure 6A-d5 .i**), as
298 previously observed in living, rhodamine-123 labeled cells (**Figure 5C**). For more precise
299 *Tb*DBF localization, we performed Ultrastructure Expansion Microscopy (U-ExM), which
300 increases the size of a sample while preserving its ultrastructure (39, 40). By this
301 approach, we show that both ^{oe}*Tb*DBF$_{::3Ty1}$ (**Figure 6B**) and the endogenous *Tb*DBF$_{::10HA}$
302 (**Figure 6C**) have a different distribution from the matrix marker (Tdh) and localizes to
303 the mitochondrial periphery. In addition, as already noticed with standard
304 immunofluorescence microscopy (**Figure 3C**), *Tb*DBF depicts a non-continuous, punctate
305 distribution within the membrane as compared to the matrix protein Tdh. These findings
306 suggest an association of the *Tb*DBF protein with mitochondrial membranes. We then
307 investigated the effect of *Tb*DBF expression in the BSF form, where the mitochondrial
308 compartment is smaller and composed of shorter and less interconnected mitochondria.
309 Overexpression of ^{oe}*Tb*DBF$_{::3Ty1}$ was monitored by western-blot (**Figure 6E**), but unlike
310 PCF, the mitochondrial structure (labeled here with mitochondrial Hsp60) was not at all
311 altered, remaining tubular and slightly reticulated like in wild-type cells (**Figure 6F**).
312 Induction over a longer period (up to 21 days) did not show mitochondrial alterations.
313 The localization of the wild-type *Tb*DBF and mutant *Tb*DBF (K141A) was also
314 investigated by electron microscopy (EM) and immunogold-labeling using an anti-Ty1
315 antibody. After induction and immunogold-labeling, both proteins are clearly localized in
316 the mitochondrion (**Figure S9A3/B3**) as compared to controls with non-induced cells
317 (**Figure S9A1/B1**), which is also confirmed by gold-particles quantification (**Figure**
318 **S9D**).
319
320 ***6 - Mitochondrial targeting and membrane anchoring of TbDBF***

321 To investigate the mechanisms ensuring mitochondrial targeting of *Tb*DBF, we first
322 addressed the two domains that may determine *Tb*DBF localization: (i) the N-terminal
323 MTS that could mediate inner membrane targeting and intermembrane space localization
324 (as the MTS of Opa1), and (ii) the C-proximal/terminal TMs that could mediate outer
325 membrane anchoring (as the TMs of Mfn). To investigate their capacity to target proteins
326 to mitochondria, we fused the MTS domain, or the two transmembrane domains of
327 *Tb*DBF, to GFP (**Figure 7A**). Fusion of the MTS at the N-terminus of GFP ($_{MTS::}$GFP) fully
328 addressed GFP to the mitochondria (**Figure 7A**). Interestingly, the size of $_{MTS::}$GFP
329 revealed by Western-blot is identical to that of cytosolic GFP without MTS (**Figure 7B**),
330 indicating that the predicted MTS maturated by Matrix Processing Peptidase (MPP)
331 (**Figure S1**) was cleaved upon import of $_{MTS::}$GFP across the inner membrane. It is to
332 note that ^{oe}*Tb*DBF$_{::3Ty1}$ and ^{oe}*Tb*DBFK141A$_{::3Ty1}$ showed the same apparent size as
333 ^{oe}*Tb*DBFΔMTS$_{::3Ty1}$ by western-blot analyses, indicating that the MTS is also cleaved in its
334 natural context (**Figure 7C**) and thus, at least the N-terminus of *Tb*DBF is imported into
335 the matrix. We then investigated the addition of the 2 C-proximal transmembrane
336 domains at the C-terminal extremity of GFP (GFP$_{::TM}$). As expected, a size shift
337 corresponding to the addition of transmembrane domains is observed by western-blot
338 (**Figure 7B**). However, in contrast to $_{MTS::}$GFP, the GFP$_{::TM}$ was not targeted to
339 mitochondria, but to unknown distinct structures, possibly membrane or ER as well as
340 the flagellum which is different from a cytosolic labeling (see GFP alone) or from a
341 mitochondrion labeling (here revealed with the anti-Tdh antibody) (**Figure 7A and**
342 **Figure S10**). Their inability to mediate mitochondrial targeting shows that the TMs of
343 *Tb*DBF do not represent mitochondrial targeting determinants like those targeting
344 mitofusins to the mitochondrial outer membrane. Their capacity to target GFP from the
345 cytosol to other organelles, suggests that they have the capacity to mediate membrane
346 anchoring. It is probable that this membrane-anchoring function is exerted within
347 mitochondria, upon MTS-mediated targeting of *Tb*DBF.
348 In order to further characterize the role and relevance of these domains on *Tb*DBF
349 localization and function, we expressed tagged *Tb*DBF-mutants without MTS

350 (^{oe}*Tb*DBFΔMTS$_{::3Ty1}$) or TMs (^{oe}*Tb*DBFLΔTM$_{::3Ty1}$) in PCF using tetracycline-induction
351 (**Figure 7D and 7G**). Conditional overexpression of both recombinant *Tb*DBF was
352 confirmed by western blot, after 3 days to 5 days of induction (**Figure 7E/7H/S8**). In
353 contrast to ^{oe}*Tb*DBF$_{::3Ty1}$, a significant proportion of ^{oe}*Tb*DBFΔMTS$_{::3Ty1}$ doesn't colocalize
354 with Tdh revealing that the N-terminal MTS is indeed required for proper mitochondrial
355 targeting of *Tb*DBF (**Figure 7F, Figure S10**). Interestingly, the labeling observed for
356 ^{oe}*Tb*DBFΔMTS$_{::3Ty1}$ is somewhat similar to the labeling of GFP$_{::TM}$ (**Figure 7A/F/S10**),
357 suggesting unspecific membrane anchoring by C-proximal TMs. The fact that part of
358 ^{oe}*Tb*DBFΔMTS$_{::3Ty1}$ still remained close to Tdh signal may show that the ΔMTS mutant is
359 also anchored to mitochondrial membranes. To analyze the localization of
360 ^{oe}*Tb*DBFΔMTS$_{::3Ty1}$ with more precision, we performed electron microscopy analysis with
361 anti-Ty1 antibody. We observed a dual localization of ^{oe}*Tb*DBFΔMTS$_{::3Ty1}$, and gold-
362 particles quantification revealed that 60% of ^{oe}*Tb*DBFΔMTS$_{::3Ty1}$ is located outside of the
363 mitochondrion and 40% inside or close to the mitochondrion membranes (**Figure**
364 **S9C/D**). MTS is therefore important for the correct localization of *Tb*DBF, but without it,
365 the protein is partially able to localize to membranes. We further observed that
366 overexpression of ^{oe}*Tb*DBFΔMTS$_{::3Ty1}$ does not alter mitochondrial structure, indicating
367 that its proper, MTS-mediated, mitochondrial localization is essential for *Tb*DBF-function
368 (**Figure 7F/Anti-Tdh and Figure S8**). We then investigated the relevance of the C-
369 proximal TMs of *Tb*DBF by overexpressing a version truncated for the TM
370 (^{oe}*Tb*DBFΔTM$_{::3Ty1}$, **Figure 7G**) and analyzed the mitochondrial shape and their
371 localization by immunofluorescence (**Figure 7I**). ^{oe}*Tb*DBFΔTM$_{::3Ty1}$ is also well over-
372 expressed (**Figure 7H and Figure S8**) and perfectly colocalizes with the mitochondrial
373 marker, like $_{MTS::}$GFP. This confirms that the N-terminal MTS sequence is sufficient for
374 mitochondrial targeting of *Tb*DBF. However, no modification of the mitochondrial shape
375 was observed (**Figure 7E3 and Figure S8**) demonstrating that the transmembrane
376 domains are required for proper function. Altogether, our data show that *Tb*DBF is
377 targeted to mitochondria by an N-terminal MTS and that C-proximal TMs are required for

378 proper function. We infer that TMs probably mediate membrane anchoring and the
379 establishment of proper membrane topology.
380
381 ***7 – Impact of TbDBF overexpression on parasite morphology/biology***
382 We then decided to characterize *Tb*DBF activity and intermitochondrial branching
383 with higher resolution. To this end, we used as serial block face scanning electron
384 microscopy (SBF-SEM), an approach allowing to characterize the overall structure of
385 membranes and organelles within the entire cell volume (18). With this technique,
386 hundreds of images are collected to perform a 3D reconstruction of the whole cell, as
387 well as spatial organization of the individual organelles within the cell. Four to five wild-
388 type and ^{oe}*Tb*DBF$_{::3Ty1}$ PCF cells were reconstructed in 3D, with a particular emphasis on
389 the mitochondrion, the nucleus, the flagellar pocket and the cell outline. We have not
390 been able to correctly identify the kinetoplast DNA on the electron microscopy images,
391 thus preventing its 3D reconstruction. However, since kDNA is in close contact with the
392 flagellar pocket, it is easy to position it. Other organelles (glycosomes, acidocalcisomes,
393 golgi, flagellum, etc.) are not represented either in order to not overload the 3D
394 representation. As expected, wild-type PCF cells showed a reticulated mitochondrion
395 along the whole cell (**Figure 8A/C**), a rather central nucleus and the flagellar pocket on
396 the posterior side. The length of the wild-type and ^{oe}*Tb*DBF$_{::3Ty1}$ cells, varies between
397 20.4±3.3 and 23±4.7 µm, respectively. As observed by fluorescence microscopy,
398 ^{oe}*Tb*DBF$_{::3Ty1}$ mitochondrion showed more areas with stronger reticulation (**Figure 8B/D,**
399 **indicated by arrows**). Unexpectedly, in some cells this reticulation is even more
400 prominent at the edges of the flagellar pocket, where the kDNA is located, as illustrated
401 in **Figure 8B/D**, an observation that we had not identified by immunofluorescence
402 microscopy approaches. This hyper-reticulated structure (leaving a few gaps in the
403 mitochondrion) forms a globular structure and probably encapsulates the kDNA (**Figure**
404 **8D, indicated by small arrows**). This structure has been already described in BSF and
405 called kDNA pocket (17), but this structure is even more prominent in the ^{oe}*Tb*DBF$_{::3Ty1}$
406 cells. It should be noted that the 3D reconstruction of ^{oe}*Tb*DBF$_{::3Ty1}$ cells required the

407 analysis of more slices in order to have a whole cell, suggesting a larger volume of the
408 cell with a width at the nucleus of ~3.96±1.19 µm for ^{oe}*Tb*DBF$_{::3Ty1}$ and ~2.51±0.28 µm
409 for wild-type cells, but no modification in the length of the parasite was observed. Wild-
410 type cells exhibit a cell volume around 53.5±6.6 µm^3, which are quite similar to the
411 volume measured in the different stages of the BSF cell cycle (cell 31-61 µm^3, (18)
412 **Figure 8E**). As anticipated, PCF mitochondrial volume is nearly doubled (4.9±1 µm^3)
413 compared to the mitochondrial volume of BSF (1.1-3 µm^3) (17, 18). As expected,
414 mitochondrial volume in cells overexpressing *Tb*DBF$_{::3Ty1}$ is almost doubled by
415 comparison to wild-type cells (**Figure 8E**) and surprisingly the whole cell volumes was
416 also increased ~1.7-fold in ^{oe}*Tb*DBF$_{::3Ty1}$ cells (**Figure 8E**).

417 On the other hand, and as presented in the introduction, the shape of the
418 mitochondrion undergoes spectacular changes during the life cycle of the parasite,
419 reflecting adaptation to different environments. These adaptations are also accompanied
420 by a profound change in their metabolism. We therefore investigated whether and how
421 an alteration of the mitochondrial structure affects the metabolism of the parasite. To
422 address this, we screened for the use of 119 different carbon and nitrogen sources in
423 parasites overexpressing or not *Tb*DBF. Two carbon sources, D-glucose and L-proline
424 (**Figure 9 and Figure S11,** n°14/114), are significantly more consumed/used in
425 ^{oe}*Tb*DBF$_{::3Ty1}$ cells compared to non-induced cells, suggesting that modifications of the
426 mitochondrial structure require increased energy consumption or to the opposite, that
427 mitochondrial shape restructuring impacts metabolism. Interestingly, ethanolamine is
428 also significantly more consumed/used in ^{oe}*Tb*DBF$_{::3Ty1}$ cells (**Figure 9 and Figure S11,**
429 n°61). This molecule is a precursor of phosphatidylethanolamine, an important
430 component of mitochondrial membranes (41), which in line with the observed increase in
431 mitochondrial complexity. Altogether these data suggest that ^{oe}*Tb*DBF$_{::3Ty1}$ cells need
432 more energy and metabolic precursors, from increased catabolism of carbon sources, to
433 fuel the increased membrane biosynthesis.

434

435 ***DISCUSSION***

436 We have identified a novel and ancestral DRP family whose first representative,
437 *Tb*DBF, has been characterized in the protozoan parasite *T. brucei*. We have
438 demonstrated that *Tb*DBF localizes to the mitochondrial periphery and is able to increase
439 mitochondrial interconnectivity in a GTPase-dependent manner. Its overexpression also
440 induces modifications in energy metabolism in the parasite, as well as membrane
441 biogenesis and shaping. We propose that mitochondrial *Tb*DBF may mediate and/or
442 enhance fusion.

443 Membrane fusion and fission are often controlled by proteins of the dynamin
444 superfamily (DRP) (42, 43). These proteins consistently have a GTPase domain and
445 contain domains required for membrane binding and oligomerization. In trypanosomes,
446 only DRPs involved in fission have been characterized, and no fusion proteins similar to
447 those of yeasts and mammals have been identified so far. This may suggest that
448 trypanosome mitochondria fuse via a machinery that differs from that characterized in
449 yeasts and mammals. Of note, the situation is similar in plants, where no fusion protein
450 similar to known fusion factors has been identified until now. Indeed, the search for
451 homologous sequences to *Tb*DBF allowed us to identify close DRP homologs in several
452 eukaryotic phyla lacking Mfn and Opa1, the fusion factors of metazoan and fungi. Unlike
453 Mfn and Opa1, that have few homologues in some prokaryotes (cyanobacterial BDLP),
454 homologues of *Tb*DBF were also identified in numerous bacterial phyla and even in
455 archaea. These data point to the existence in these organisms of a novel machinery
456 involved in membrane fusion, shaping and/or remodeling that is not present in
457 *Opisthokonta* and *Plantae* but still present in numerous prokaryotes. While studies of
458 yeast and mammalian DRPs provide information about their functions and structures,
459 little is known about bacterial DRPs, especially their cellular role. Indeed, some bacterial
460 DRPs have been associated with a variety of processes involving membranes *in vivo*,
461 such as a surveillance mechanism for membrane punctures caused by antibiotics and
462 bacteriophages (44, 45), membrane vesicle formation (46) or cytokinesis by promoting
463 membrane curvature at the septum (47, 48). In addition, studies of the *Bacillus subtilis*

464 DRP DynA have shown that this protein can promote membrane fusion *in vitro* (49). The
465 mechanism by which the fusion operates is not yet known, but bacterial DRPs are
466 probably recruited to the sites where membrane fusion is needed (48, 50). Interestingly,
467 structural analysis of *Campylobacter jejuni* DLP1/DLP2 proteins allowed to propose a
468 mechanism explaining how these proteins attach and bind distant and opposing
469 membranes (51). Unfortunately, the cellular function of *C. jejuni* DLP1/DLP2 is currently
470 unknown. DRPs identified in this study have not yet been characterized and no
471 information on their localization and function is available. However, among the identified
472 organisms, we found, with the second-best score (E-Value 2e-80, **Table S1**), the
473 bacteria of the phylum Planctomycetes which are somewhat particular organisms.
474 Indeed, these bacteria contain a compartmentalized cytosol, separated by an
475 intracytoplasmic membrane (52), in some cases surrounding the nucleus (53) or forming
476 an anammoxosome, a pseudo-mitochondrion that is responsible for the production of
477 energy (54, 55). It is then conceivable that the identified protein in Planctomycetes
478 (*Pb*DBF, **Figure 2 and S3**) is involved in membrane structuring.
479 The role of *Tb*DBF in mitochondrial shaping was then confirmed by its
480 overexpression in PCF. Indeed, overexpressed *Tb*DBF modifies the structure of the
481 mitochondrion, with a very strong increase in connections. Moreover, the inactivation of
482 its GTPase domain (K141A mutation) also confirms its belonging to the large family of
483 dynamins. Interestingly, a similar link between hyperconnection of a branching network
484 and increased fusion processes has been reported in filamentous fungi, which grow as
485 interconnected branching networks (56). It is therefore tempting to speculate that, in
486 trypanosomes, excess *Tb*DBF increases the interconnectivity of mitochondrial networks
487 by enhanced fusion. The absence of fragmentation observed upon partial or total
488 inactivation of *Tb*DBF expression was rather expected and suggests that trypanosomes
489 differ from mammalian and yeast cells by the absence or a very low level of
490 regular/permanent mitochondrial fission. This is in agreement with previous studies
491 suggesting that fission only occurs during cell division (21, 28). It should also be kept in
492 mind that other proteins could be involved in the structuring of mitochondria as shown

493 by studies on mitochondrial outer membrane proteome in *T. brucei* (57, 58) and the
494 presence of mitochondrial complexes such as recently characterized MICOS (59). It
495 should be noted that *Tb*DBF seems to be part of a new fusion mechanism, so its
496 inactivation may not have the same effects as for Mfn or Opa1. It is also possible that
497 subtle changes in mitochondrial structure are present, but that we were not able to
498 reveal with our approaches. Another intriguing point is the absence of phenotype in
499 response to overexpression of *Tb*DBF in the BSF, which seems to reflect the relatively low
500 dynamics of the mitochondrial structuration in these parasitic forms. It is possible that
501 *Tb*DBF interacts with other partners, in a possible branching complex, that might only be
502 expressed in the PCF. However, one cannot exclude that overexpression of *Tb*DBF is not
503 high enough to initiate an increase in interconnectivity.

504 Using several microscopy approaches, we have shown that *Tb*DBF is localized in the
505 mitochondrion and more precisely in the mitochondrial membranes. *Tb*DBF contains two
506 domains involved in its accurate mitochondrial addressing, an N-terminal sequence
507 (MTS) and two C-terminal transmembrane domains. Proteins with an N-terminal MTS
508 are mainly fully imported into the mitochondrial matrix, however, some of them, such as
509 Opa1 and Apoptosis-inducing factor (AIF) face the inner membrane (60). Indeed, Opa1
510 and AIF localize mainly to the IMS due to its TM domain located in close proximity to the
511 MTS, interrupting transport across the inner membrane, which is not the case for *Tb*DBF.
512 Moreover, *Tb*DBF has a functional MTS, which is cleaved in the mitochondrial matrix and
513 its absence impacts the activity of the protein, suggesting that at least part of the protein
514 crosses OMM and IMM. However, with an MTS-less construct, the protein is still partially
515 associated to the mitochondrion and other membranes through its two C-terminal
516 transmembrane domains. It should be noted that the targeting specificity of C-terminal
517 TM domains is often determined by the amino acids flanking the TMs (61, 62) which
518 could explain the remaining *Tb*DBF protein in mitochondrion when the MTS was deleted.
519 *Tb*DBF TM domains should therefore be considered as membrane-anchoring domains.
520 Interestingly, the structure prediction of *Tb*DBF by Alphafold (63) suggests that the two
521 TM domains form a loop that may allow anchoring in the inner membrane with a possible

522 orientation of the remaining protein on the matrix side (**Figure 10**). This orientation is
523 also probably similar to the prokaryotic DBFs which could also be anchored in the plasma
524 membrane and facing the cytosol. Recently, Sheik *et al.* (22) clearly demonstrated that
525 expression of a potential DRP from giant virus in *T. brucei* PCF strongly affects
526 mitochondrial morphology within the matrix, with a close association with the inner
527 membrane. This contrasts with the mode of action of human or yeast mitofusins, which
528 are involved in the remodeling of mitochondrial outer and inner membranes, but never
529 via the matrix side. All of these results point to a complex or even unique targeting and
530 membrane topology of *Tb*DBF, different from those observed for mammalian and fungi
531 OM and IM fusion factors.

532 In many eukaryotes, mitochondria display a dynamic behaviour of constant fission
533 and fusion, with the size, appearance and organization of mitochondrial membranes
534 varying between species, tissues and physiological conditions (7). Although there is
535 considerable convincing evidence that mitochondrial dynamics and bioenergetics are
536 linked, the precise relationship between the two is still not known (6-8). It is therefore
537 tempting to assume that such tight connections regulate not only mitochondrial function
538 and energy metabolism, but also the life cycle and pathogenic potential of trypanosomes.
539 In order to identify possible metabolic variations induced by *Tb*DBF overexpression, we
540 screened 119 molecules that could be used by parasites as carbon and energy sources.
541 Only 3 molecules appeared to be more used/consumed in cells with altered mitochondria,
542 i.e., glucose, proline and ethanolamine. Glucose and proline are the two main carbon
543 sources that trypanosomes use in the mammalian host and the insect vector,
544 respectively. This suggests a greater energy demand, required either to change the
545 mitochondrial structure and/or to increase the mitochondrial content. The third molecule,
546 ethanolamine, is probably not a carbon source *per se*, but reflects a change in
547 phospholipid metabolism and more specifically in phosphatidylethanolamine (PE), which
548 together with phosphatidylcholine (PC), are the main constituents of eukaryotic cell
549 membranes. PE is preferentially distributed in the inner leaflet of mitochondrial
550 membranes and plays an essential role in mitochondrial functions (64, 65) by

551 maintaining the mitochondrial morphology (66-68). Indeed, PE is a fusogenic
552 phospholipid that confers negative curvature to the mitochondrial membrane (69) and
553 has been proposed to play important roles in membrane fusion involving the mitofusin
554 Mfn (70). In PCF *T. brucei*, PE and PC are synthesized exclusively through the Kennedy
555 pathway (71). Mutations in lipid composition result in alterations in mitochondrial
556 morphology and inhibition of respiration (72) (73). Remarkably, RNAi-mediated down-
557 regulation of ethanolamine phosphate cytidylyltransferase expression, the second
558 enzyme in the Kennedy pathway, has been shown to disrupt mitochondrial morphology
559 and ultrastructure in *T. brucei*. The most immediate effect was a change in mitochondrial
560 morphology and disruption of the inner mitochondrial membrane topology (74). Since PE
561 is essential for mitochondrial morphology, the increased ethanolamine
562 utilization/consumption in *Tb*DBF-overexpressing parasites likely reflects increased
563 membrane lipid biogenesis to support the alterations in mitochondrial structure. SBF-SEM
564 analysis and 3D reconstruction of parasites expressing *Tb*DBFL showed a significant
565 increase in mitochondrial membrane biogenesis with an almost doubling of the
566 mitochondrial volume. This increased membrane biogenesis is particularly evident in the
567 vicinity of the kDNA, which is completely enveloped by a hyper-reticulated globular
568 mitochondrial structure. More work is needed to determine whether this part of the
569 mitochondrion is a preferential place for membrane biogenesis. It is therefore likely that
570 the increase in membrane biogenesis is not limited to the mitochondrial membranes, but
571 also affects the other cell membranes which may explain the significant increase of the
572 cell volume observed and thus the cellular surface. However, this increase in volume
573 does not affect the parasite's growth rate, implying that the increase in volume is
574 disconnected from mechanisms regulating cell division. More work is now required to
575 understand how *Tb*DBF induces these structural and metabolic changes, as well as its
576 mode of action.

577 In conclusion, all these results clearly revealed the presence of a novel and
578 ancestral machinery involved in mitochondrial branching in trypanosomes. In addition,

579 the wide conservation of these DRPs in many eukaryotic, bacterial and archaeal genomes
580 suggests an important role in the biology of these organisms.

581 ## *MATERIALS AND METHODS*

582 ### *Trypanosomes and cell cultures*

583 The PCF of *T. brucei* EATRO1125.T7T (TetR-HYG-T7RNAPOL-NEO, where TetR stands for
584 tetracycline resistance, HYG for hygromycin, T7RNAPOL for RNA polymerase T7, and NEO
585 for neomycin) was cultured at 27°C with 5% CO_2 in SDM79 medium containing 10%
586 (vol/vol) heat-inactivated fetal calf serum, 5 µg/ml hemin, 25 µg/ml hygromycin and 10
587 µg/mL neomycin. The bloodstream form of *T. brucei* 427 90-13 (TetR-HYG-T7RNAPOL-
588 NEO) was cultured at 37°C with 5% CO_2 in Iscove's modified Dulbecco's medium (IMDM)
589 supplemented with 10% (vol/vol) heat-inactivated fetal calf serum (FCS), 0.2 mM β-
590 mercaptoethanol, 36 mM $NaHCO_3$, 1 mM hypoxanthine, 0.16 mM thymidine, 1 mM
591 sodium pyruvate, 0.05 mM bathocuproine, 1.5 mM L-cysteine (75), 5 µg/ml hygromycin
592 and 2,5 µg/mL neomycin. Overexpression cell lines were induced with tetracycline (10
593 µg/mL for BSF and 1 µg/mL for PCF). Growth was monitored by daily cell counting with
594 the cytometer Guava® Muse® and Guava® easyCyte™.

595

596 ### *Endogenous tagging and overexpression of TbDBF*

597 For endogenous gene tagging, primers were designed as described in (31) and PCR was
598 performed using pPOTv7 vector as template. The pPOT used here was pPOTv7 for C-
599 terminus 10xHA tagging (blasticidin resistance). For overexpression, DBF gene
600 (Tb427.07.2410) was inserted in both pLew100 (phleomycine resistance) (76) and
601 pHD1336 (blasticidin resistance) (77) expression vectors. Fragments were amplified and
602 cloned into *Hin*dIII and *Xba*I restrictions sites of the pLew100 and into *Hin*dIII and
603 *Bam*HI restrictions sites of the pHD1336 expression vectors. In addition, a 3xTy1 tag was
604 added at the C-terminus of the protein in the pLew100-*Tb*DBF, using the *Xba*I and
605 *Bam*HI restrictions sites. The truncated version of *Tb*DBF without the first 41 amino acids
606 (*Tb*DBFΔMTS) and without the two trans-membranes domain (*Tb*DBFΔTM) were amplified
607 and cloned in the pLew100 with a 3xTy1 tag as previously described. Catalytic mutant
608 K141 was replaced by an alanine, using PCR approach (78) and PCR product cloned in
609 the pLew100 with a 3xTy1 tag. EATRO1125.T7T PCF was transfected using Amaxa

610 Nucleofector®II, program X-001 and selected in SDM79 containing 25 µg/ml hygromycin
611 10 µg/mL neomycin and 5 µg/mL phleomycin. 427 90-13 BSF was transfected using the
612 same conditions and selected in IMDM containing 5 µg/ml hygromycin, 2,5 µg/mL
613 neomycin and 5 µg/mL blasticidin. Primers used for the constructions are presented in
614 supplemental **Table S2**.
615
616 ***Endogenous tagging and inactivation of TbDBF by CRISPR-Cas9***
617 Endogenous tagging and inactivation of *Tb*DBF was achieved by CRISPR Cas9 technology
618 according Soares Medeiros et *al.* (35) but using *Sp*Cas9 instead of *Sa*Cas9 (more detailed
619 description of optimized and adapted protocols will be published separately). Briefly,
620 inactivation of the *Tb*DBF was achieved by inserting the resistant marker puromycin
621 (Pac) or a small sequence encoding for a *Bam*HI restriction site plus 6 successive stop
622 codons, flanked by 50 bp homologous to the 5' and 3' *Tb*DBF sequences from the Cas9
623 cutting site. Similar approaches have been performed for endogenous tagging with the
624 insertion of a sequence encoding 3xTy1 or 3xHA. The EATRO1125.T7T PCF and the 427
625 90.13 BSF ($1x10^6$ cells) were respectively transfected, using Amaxa nucleofectorII, with
626 1 µg of purified cassette (puromycin resistance marker, Stop*Bam*H1Stop, 3xTy1 or
627 3xHA), 30 µg Cas9 protein from IDT and pre-annealing TracrRNA (0.4 µmol) and gRNA
628 (0.4 µmol). Cells were transfected using program X-001 and selected or not with
629 puromycin (SDM79, 1 µg/mL, or IMDM 0.1 µg)/mL). Cells were cloned by using a cell
630 sorter (TBM Core facility), and selection of double inactivated *Tb*DBF gene (*Tb*DBF$^{-/-}$) or
631 endogenously tagged clones was done by DNA extraction, with NucleoSpin Blood
632 (Macherey-Nagel) and PCR amplification, see supplemental **Table S2**. Guide RNA were
633 designed using EuPaGDT, from http://tritrypdb.org. Primers and guide RNA used are
634 synthetized by Integrated DNA Technologies (IDT) and listed in supplemental **Table S2**.
635
636 ***Down-regulation of TbDBF gene expression***
637 Down-regulation of DBF expression by RNAi in PCF was achieved by expression of stem-
638 loop "sense/antisense" RNA molecules targeting a 400-bp fragment of the DBF gene

639 introduced into the pLew100 tetracycline-inducible expression vector. A PCR-amplified
640 450-bp fragment, containing the antisense DBF sequence was inserted between *Xho*I and
641 *Bam*HI restriction sites of the pLew100 plasmid. Then, the separate 400-bp PCR-
642 amplified fragment containing the sense DBF sequence was inserted upstream of the
643 antisense sequence, using *Hin*dIII and *Xho*I restriction sites. The resulting plasmid,
644 pLew100-DBF-SAS, contains a sense and antisense version of the DBF fragment
645 separated by a 50-bp fragment. The EATRO1125 PCF was transfected with the pLew100-
646 DBF-SAS and cells were selected in SDM79 medium containing 25 µg/ml hygromycin, 10
647 µg/mL neomycin and 5 µg/mL phleomycin. Expression of the RNAi was induced by
648 tetracycline (1 µg/mL).
649 Down-regulation of DBF expression by RNAi in BSF was achieved exactly as described
650 (29) with a 280-bp fragment derived from the *Tb*DBF open reading frame inserted into
651 the p2T7-177 plasmid (79). Linearized plasmid was transfected in *T. brucei* 427 90-13
652 (TetR-HYG-T7RNAPOL-NEO) BSF cells. Expression of the RNAi was induced by
653 tetracycline (10 µg/mL). Primers used for the constructions are presented in
654 supplemental **Table S2**.
655
656 ***Mitochondria staining on living cells***
657 Rhodamine-123 (30 µg/mL) was added on cell culture ($5x10^6$ - $1x10^7$ cells per mL) for 15
658 min at room temperature, then cells were washed twice with PBS and spread on slides.
659 Images were acquired with MetaMorph software on Axioplan 2 microscope and processed
660 with ImageJ.
661
662 ***Immunofluorescence***
663 Cells were washed twice with PBS, then fixed with 2% paraformaldehyde (PFA) for 10
664 min at room temperature and 0.1mM Glycine was added 10 min to stop the reaction. The
665 cells were spread on slides and permeabilized with 0.05% triton X-100. After incubation
666 in PBS containing 4% bovine serum albumin (BSA) 20 min, cells were incubated for 1
667 hour with primary antibodies diluted in PBS-BSA 4%, washed 4 times with PBS and

668 incubated for 45 min with secondary antibodies diluted in PBS-BSA 4% followed by three
669 washes. Then, kinetoplasts and nuclei were labelled with DAPI (10 µg/mL) for 5 min.
670 Slides were washed 3 times with PBS and mounted with SlowFade Gold (Molecular
671 probes). Images were acquired with MetaMorph software on Zeiss Imager Z1 or Axioplan
672 2 microscope and processed with ImageJ.
673
674 ***Ultrastructure Expansion Microscopy (UExM)***
675 The protocol of UExM realized exactly as described by Casas et *al.* 2022
676 (dx.doi.org/10.17504/protocols.io.bvwqn7dw). An expansion factor was determined
677 using the ratio between the size of the coverslip (12mm) and the size of the gels after
678 the first expansion. Images were acquired on a confocal Leica SP5-MP (Bordeaux
679 Imaging Center) using a 63X oil objective and processed with ImageJ.
680
681 ***Immunoelectron microscopy***
682 Harvested cells were placed on the surface of formvar-coated copper grids (400 mesh).
683 Each loop was quickly submersed in liquid propane (−180°C) and transferred into a
684 precooled solution of 0.1% uranyl acetate in dry acetone for 3 days at -82°C. Samples
685 were rinsed with acetone at -20°C, and embedded progressively at -20°C in LR Gold
686 resin (EMS, USA). Resin polymerization was carried out at -20°C for 7 days under UV
687 illumination. Ultrathin LR Gold sections were collected on nickel grids coated with
688 formvar. Sections were first incubated for 15 min with NH_4Cl 500mM in Tris-buffered
689 saline (TBS) pH7.8, blocked 2x10 min with 2% BSA in TBS pH 7.8. The grids were
690 incubated 1 hour at room temperature with anti Ty1 antibody diluted to 1:200 in TBS
691 containing 2% BSA rinsed with TBS containing 2% BSA and with TBS containing 1% BSA.
692 The samples were then incubated for 1 hour at room temperature with anti-mouse IgG
693 diluted to 1:20 conjugated to 10 nm gold particles (BioCell). The sections were rinsed
694 with TBS containing 1% BSA, and fix with 1% glutaraldehyde in TBS. After rinsing with
695 TBS, grids were contrasted through a 5 min incubation with 2% uranyl acetate in water,
696 followed by 1 min incubation with 1% lead citrate. Observations were performed on a

697 HITACHI 7650 electron microscope operated at 80 KV with a Gatan-11 MPx camera (PIE
698 Bordeaux Imaging Center).
699
700 ***SBF-SEM***
701 Cells were prepared as described by Blancard and Salin (80) except for freeze-
702 substitution medium (0.1% potassium permanganate for 24 h followed by 0.1% tannic
703 acid for 24 h, and 2% osmium tetroxide with 1% uranyl acetate for 3 days). Resin-
704 embedded samples were trimmed, mounted onto stubs and placed into a Zeiss
705 GeminiSEM300 with a fitted Gatan 3View2XP system (Gatan, Abingdon, UK). Serial
706 images of the block face were recorded at an accelerating voltage of 1.2 kV. All images
707 were taken with the following scanning settings: Pixel size 10 nm, pixel time 5 µs, slice
708 thickness 50 nm (Z-slice), image size 5000x5000. Between 700 and 900 images were
709 collected for each run. Images were collected from Back scattered electron with a specific
710 BSE Detector (On point - Gatan Inc., Pleasanton, CA, USA) using the software Digital
711 Micrograph (Gatan). Images were combined to form a single stack. Data processing and
712 statistical analysis: Segmentation was conducted using AMIRA (versions 5.2.0
713 Thermofisher Scientific). Manual segmentation of cells and organelles were conducted
714 using the brush tool and was based on ultrastructural characteristics specific to each
715 organelle. Each organelle was segmented using the organelle membrane as the outer
716 edge. Surface models were produced for each segmented organelle. Volumes of
717 organelles were automatically generated from the surface renderings of segmented data.
718
719 ***Western-blot***
720 Total protein extracts ($5x10^6$ cells) were separated by SDS-PAGE (10%) and
721 immunoblotted on TransBlot Turbo Midi-size PVDF Membranes (Bio-Rad).
722 Immunodetection was performed using the primary antibodies, diluted in PBS-Tween-
723 Milk (0.05% Tween20, 5% skimmed milk powder), summarized in supplemental **Table**
724 **S3**. Revelation was performed using a second antibody coupled to the HRP and the
725 Clarity Western enhanced-chemiluminescence (ECL) substrate as describes by the

726 manufacturer (Bio-Rad). Images were acquired and analyzed with the ImageQuant Las
727 4000 luminescent image analyzer.
728
729 ***Biolog***
730 Biolog Phenotype MicroArrays™ provide an easy-to-use technology for scanning and
731 measuring the energy metabolism pathways present in a wide range of *in vitro* cultured
732 cell types. The metabolic pathway activities are assayed with a simple colorimetric
733 reagent that measures redox energy produced when a cell oxidizes a chemical
734 (Tetrazolium reduction). Standard protocol described by the manufacturer (Biolog) has
735 been used with the following modifications: cells were resuspended in Biolog IF-M1 buffer
736 at $1x10^7$ cells per mL and 50 µL of this cell suspension were pre-incubated in each well of
737 the PM-M1 or PM-M2 plates for 1 hours at 27°C with 5% CO_2. Then, 10 µL of Biolog Dye
738 Mix (Mix MB) was added to all plate wells and load into the Omnilog® for kinetic reading
739 for 18 hours at 27°C or endpoint measurement at 590 nm with a microplate reader after
740 18 hours.
741
742 ***Quantification of Mitochondrial junctions - ImageJ macro***
743 To quantify number of mitochondrial junctions, an ImageJ macro was developed with the
744 help of the Bordeaux Imaging Center (BIC). The script is presented in supplemental
745 Materials and Methods data **MMS1**.
746
747 ***Statistical analysis***
748 Experiments were performed at least in triplicates. Statistical analyses were performed
749 using Prism (GraphPad) software. The results are presented as mean ± S.D. Where
750 indicated the results were subjected to two-sided student's t-test to determine statistical
751 differences against the indicated group (Confidence interval 95% - P-value style: 0.1234
752 (ns); 0.0332 (*); 0.0021 (**); 0.0002 (***); <0.0001 (****)).
753
754 ***Structural prediction software and sequence analysis***

755 Structure predictions were performed using PSIPRED
756 ("http://bioinf.cs.ucl.ac.uk/psipred/") (81) and prediction of mitochondrial targeting
757 sequences by various algorythms (MitoprotII, MitoFates and iPSORT) (82). Phylogeny
758 analysis was performed with Geneious software using default parameters and the
759 neighbor-joining method was used for tree calculation.

760 ***ACKNOWLEDGMENTS***

761 We thank Keith Gull (University of Manchester) for providing us the anti-Ty1 and anti-
762 PFR antibodies and Derrick Robinson, Mélanie Bonhivers, Elina Casas and Nicolas
763 Landrein (University of Bordeaux) for the pPOTv7 expression vector and extremely
764 valuable help in the expansion microscopy experiment. Cell sorter analysis were
765 performed at the TBMCore facility (FACSility) on BD FACSAria™ III Sorter and we thank
766 Atika Zouine for data acquisition and interpretation. We also thanks Bordeaux Imaging
767 Center (BIC), which is a member of the FranceBioImaging national infrastructure (ANR-
768 10-INBS-04), for helping us to design the ImageJ macro and microscopy acquisitions.

769 ***REFERENCES***

770 1. Bohringer S, Hecker H. Quantitative ultrastructural investigations of the life cycle
771 of Trypanosoma brucei: a morphometric analysis. J Protozool. 1975;22(4):463-7.

772 2. Priest JW, Hajduk SL. Developmental regulation of Trypanosoma brucei
773 cytochrome c reductase during bloodstream to procyclic differentiation. Mol Biochem
774 Parasitol. 1994;65(2):291-304.

775 3. van Hellemond JJ, Opperdoes FR, Tielens AG. The extraordinary mitochondrion
776 and unusual citric acid cycle in Trypanosoma brucei. Biochem Soc Trans. 2005;33(Pt
777 5):967-71.

778 4. Michels PA, Bringaud F, Herman M, Hannaert V. Metabolic functions of glycosomes
779 in trypanosomatids. Biochim Biophys Acta. 2006;1763(12):1463-77.

780 5. Matthews KR. The developmental cell biology of Trypanosoma brucei. J Cell Sci.
781 2005;118(Pt 2):283-90.

782 6. Duvezin-Caubet S, Jagasia R, Wagener J, Hofmann S, Trifunovic A, Hansson A, et
783 al. Proteolytic processing of OPA1 links mitochondrial dysfunction to alterations in
784 mitochondrial morphology. J Biol Chem. 2006;281(49):37972-9.

785 7. Sauvanet C, Duvezin-Caubet S, di Rago JP, Rojo M. Energetic requirements and
786 bioenergetic modulation of mitochondrial morphology and dynamics. Semin Cell Dev Biol.
787 2010;21(6):558-65.

788 8. Silva Ramos E, Larsson NG, Mourier A. Bioenergetic roles of mitochondrial fusion.
789 Biochim Biophys Acta. 2016;1857(8):1277-83.

790 9. Chan DC. Fusion and fission: interlinked processes critical for mitochondrial
791 health. Annual review of genetics. 2012;46:265-87.

792 10. Westermann B. Mitochondrial fusion and fission in cell life and death. Nat Rev Mol
793 Cell Biol. 2010;11(12):872-84.

794 11. Sesaki H, Adachi Y, Kageyama Y, Itoh K, Iijima M. In vivo functions of Drp1:
795 lessons learned from yeast genetics and mouse knockouts. Biochim Biophys Acta.
796 2014;1842(8):1179-85.

797 12. Otera H, Ishihara N, Mihara K. New insights into the function and regulation of
798 mitochondrial fission. Biochim Biophys Acta. 2013;1833(5):1256-68.

799 13. Malka F, Guillery O, Cifuentes-Diaz C, Guillou E, Belenguer P, Lombes A, et al.
800 Separate fusion of outer and inner mitochondrial membranes. EMBO Rep.
801 2005;6(9):853-9.

802 14. Song Z, Ghochani M, McCaffery JM, Frey TG, Chan DC. Mitofusins and OPA1
803 mediate sequential steps in mitochondrial membrane fusion. Mol Biol Cell.
804 2009;20(15):3525-32.

805 15. Legros F, Lombes A, Frachon P, Rojo M. Mitochondrial fusion in human cells is
806 efficient, requires the inner membrane potential, and is mediated by mitofusins. Mol Biol
807 Cell. 2002;13(12):4343-54.

808 16. Bertholet AM, Delerue T, Millet AM, Moulis MF, David C, Daloyau M, et al.
809 Mitochondrial fusion/fission dynamics in neurodegeneration and neuronal plasticity.
810 Neurobiol Dis. 2016;90:3-19.

811 17. Jakob M, Hoffmann A, Amodeo S, Peitsch C, Zuber B, Ochsenreiter T.
812 Mitochondrial growth during the cell cycle of Trypanosoma brucei bloodstream forms. Sci
813 Rep. 2016;6:36565.

814 18. Hughes L, Borrett S, Towers K, Starborg T, Vaughan S. Patterns of organelle
815 ontogeny through a cell cycle revealed by whole-cell reconstructions using 3D electron
816 microscopy. J Cell Sci. 2017;130(3):637-47.

817 19. Gibson W, Crow M, Kearns J. Kinetoplast DNA minicircles are inherited from both
818 parents in genetic crosses of Trypanosoma brucei. Parasitol Res. 1997;83(5):483-8.

819 20. Esseiva AC, Chanez AL, Bochud-Allemann N, Martinou JC, Hemphill A, Schneider
820 A. Temporal dissection of Bax-induced events leading to fission of the single
821 mitochondrion in Trypanosoma brucei. EMBO Rep. 2004;5(3):268-73.

822 21. Chanez AL, Hehl AB, Engstler M, Schneider A. Ablation of the single dynamin of T.
823 brucei blocks mitochondrial fission and endocytosis and leads to a precise cytokinesis
824 arrest. J Cell Sci. 2006;119(Pt 14):2968-74.

825 22. Sheikh S, Panek T, Gahura O, Tyc J, Zahonova K, Lukes J, et al. A Novel Group of
826 Dynamin-Related Proteins Shared by Eukaryotes and Giant Viruses Is Able to Remodel
827 Mitochondria From Within the Matrix. Mol Biol Evol. 2023;40(6).

828 23. Sesaki H, Jensen RE. Division versus fusion: Dnm1p and Fzo1p antagonistically
829 regulate mitochondrial shape. J Cell Biol. 1999;147(4):699-706.

830 24. Bleazard W, McCaffery JM, King EJ, Bale S, Mozdy A, Tieu Q, et al. The dynamin-
831 related GTPase Dnm1 regulates mitochondrial fission in yeast. Nature cell biology.
832 1999;1(5):298-304.

833 25. DiMaio J, Ruthel G, Cannon JJ, Malfara MF, Povelones ML. The single
834 mitochondrion of the kinetoplastid parasite Crithidia fasciculata is a dynamic network.
835 PLoS ONE. 2018;13(12):e0202711.

836 26. Logan DC. Plant mitochondrial dynamics. Biochim Biophys Acta. 2006;1763(5-
837 6):430-41.

838 27. Arimura SI. Fission and Fusion of Plant Mitochondria, and Genome Maintenance.
839 Plant Physiol. 2018;176(1):152-61.

840 28. Morgan GW, Goulding D, Field MC. The single dynamin-like protein of
841 Trypanosoma brucei regulates mitochondrial division and is not required for endocytosis.
842 J Biol Chem. 2004;279(11):10692-701.

843 29. Vanwalleghem G, Fontaine F, Lecordier L, Tebabi P, Klewe K, Nolan DP, et al.
844 Coupling of lysosomal and mitochondrial membrane permeabilization in trypanolysis by
845 APOL1. Nature communications. 2015;6:8078.

846 30. Dean S, Sunter JD, Wheeler RJ. TrypTag.org: A Trypanosome Genome-wide
847 Protein Localisation Resource. Trends Parasitol. 2017;33(2):80-2.

848 31. Dean S, Sunter J, Wheeler RJ, Hodkinson I, Gluenz E, Gull K. A toolkit enabling
849 efficient, scalable and reproducible gene tagging in trypanosomatids. Open Biol.
850 2015;5(1):140197.

851 32. Urbaniak MD, Guther ML, Ferguson MA. Comparative SILAC proteomic analysis of
852 Trypanosoma brucei bloodstream and procyclic lifecycle stages. PLoS ONE.
853 2012;7(5):e36619.

854 33. Millerioux Y, Ebikeme C, Biran M, Morand P, Bouyssou G, Vincent IM, et al. The
855 threonine degradation pathway of the Trypanosoma brucei procyclic form: the main
856 carbon source for lipid biosynthesis is under metabolic control. Mol Microbiol.
857 2013;90(1):114-29.

858 34. Nunnari J, Marshall WF, Straight A, Murray A, Sedat JW, Walter P. Mitochondrial
859 transmission during mating in Saccharomyces cerevisiae is determined by mitochondrial
860 fusion and fission and the intramitochondrial segregation of mitochondrial DNA. Mol Biol
861 Cell. 1997;8(7):1233-42.

862 35. Soares Medeiros LC, South L, Peng D, Bustamante JM, Wang W, Bunkofske M, et
863 al. Rapid, Selection-Free, High-Efficiency Genome Editing in Protozoan Parasites Using
864 CRISPR-Cas9 Ribonucleoproteins. MBio. 2017;8(6).

865 36. Hales KG, Fuller MT. Developmentally regulated mitochondrial fusion mediated by
866 a conserved, novel, predicted GTPase. Cell. 1997;90(1):121-9.

867 37. Hermann GJ, Thatcher JW, Mills JP, Hales KG, Fuller MT, Nunnari J, et al.
868 Mitochondrial fusion in yeast requires the transmembrane GTPase Fzo1p. J Cell Biol.
869 1998;143(2):359-73.

870 38. Santel A, Frank S, Gaume B, Herrler M, Youle RJ, Fuller MT. Mitofusin-1 protein is
871 a generally expressed mediator of mitochondrial fusion in mammalian cells. J Cell Sci.
872 2003;116(Pt 13):2763-74.

873 39. Gambarotto D, Hamel V, Guichard P. Ultrastructure expansion microscopy (U-
874 ExM). Methods in cell biology. 2021;161:57-81.

875 40. Amodeo S, Kalichava A, Fradera-Sola A, Bertiaux-Lequoy E, Guichard P, Butter F,
876 et al. Characterization of the novel mitochondrial genome segregation factor TAP110 in
877 Trypanosoma brucei. J Cell Sci. 2021;134(5).

878 41. Richmond GS, Gibellini F, Young SA, Major L, Denton H, Lilley A, et al. Lipidomic
879 analysis of bloodstream and procyclic form Trypanosoma brucei. Parasitology.
880 2010;137(9):1357-92.

881 42. Daumke O, Praefcke GJ. Invited review: Mechanisms of GTP hydrolysis and
882 conformational transitions in the dynamin superfamily. Biopolymers. 2016;105(8):580-
883 93.

884 43. Ramachandran R, Schmid SL. The dynamin superfamily. Curr Biol.
885 2018;28(8):R411-R6.

886 44. Sawant P, Eissenberger K, Karier L, Mascher T, Bramkamp M. A dynamin-like
887 protein involved in bacterial cell membrane surveillance under environmental stress.
888 Environ Microbiol. 2016;18(8):2705-20.

889 45. de Sousa Borges A, Scheffers DJ. Bacterial dynamin as a membrane puncture
890 repair kit. Environ Microbiol. 2016;18(8):2298-301.

891 46. Michie KA, Boysen A, Low HH, Moller-Jensen J, Lowe J. LeoA, B and C from
892 enterotoxigenic Escherichia coli (ETEC) are bacterial dynamins. PLoS ONE.
893 2014;9(9):e107211.

894 47. Schlimpert S, Wasserstrom S, Chandra G, Bibb MJ, Findlay KC, Flardh K, et al.
895 Two dynamin-like proteins stabilize FtsZ rings during Streptomyces sporulation. Proc Natl
896 Acad Sci U S A. 2017;114(30):E6176-E83.

897 48. Bramkamp M. Structure and function of bacterial dynamin-like proteins. Biol
898 Chem. 2012;393(11):1203-14.

899 49. Burmann F, Ebert N, van Baarle S, Bramkamp M. A bacterial dynamin-like protein
900 mediating nucleotide-independent membrane fusion. Mol Microbiol. 2011;79(5):1294-
901 304.

902 50. Jimah JR, Hinshaw JE. Structural Insights into the Mechanism of Dynamin
903 Superfamily Proteins. Trends Cell Biol. 2019;29(3):257-73.

904 51. Liu J, Noel JK, Low HH. Structural basis for membrane tethering by a bacterial
905 dynamin-like pair. Nature communications. 2018;9(1):3345.

906 52. Lindsay MR, Webb RI, Fuerst JA. Pirellulosomes: a new type of membrane-
907 bounded cell compartment in planctomycete bacteria of the genus Pirellula. Microbiology
908 (Reading). 1997;143(3):739-48.

909 53. Fuerst JA, Webb RI. Membrane-bounded nucleoid in the eubacterium Gemmata
910 obscuriglobus. Proc Natl Acad Sci U S A. 1991;88(18):8184-8.

911 54. Jogler C. The bacterial 'mitochondrium'. Mol Microbiol. 2014;94(4):751-5.

912 55. Neumann S, Wessels HJ, Rijpstra WI, Sinninghe Damste JS, Kartal B, Jetten MS,
913 et al. Isolation and characterization of a prokaryotic cell organelle from the anammox
914 bacterium Kuenenia stuttgartiensis. Mol Microbiol. 2014;94(4):794-802.

915 56. Herzog S, Schumann MR, Fleissner A. Cell fusion in Neurospora crassa. Current
916 opinion in microbiology. 2015;28:53-9.

917 57. Niemann M, Wiese S, Mani J, Chanfon A, Jackson C, Meisinger C, et al.
918 Mitochondrial outer membrane proteome of Trypanosoma brucei reveals novel factors
919 required to maintain mitochondrial morphology. Mol Cell Proteomics. 2013;12(2):515-28.

920 58. Povelones ML, Tiengwe C, Gluenz E, Gull K, Englund PT, Jensen RE. Mitochondrial
921 shape and function in trypanosomes requires the outer membrane protein, TbLOK1. Mol
922 Microbiol. 2013;87(4):713-29.

923 59. Kaurov I, Vancova M, Schimanski B, Cadena LR, Heller J, Bily T, et al. The
924 Diverged Trypanosome MICOS Complex as a Hub for Mitochondrial Cristae Shaping and
925 Protein Import. Curr Biol. 2018;28(21):3393-407 e5.

926 60. Otera H, Ohsakaya S, Nagaura Z, Ishihara N, Mihara K. Export of mitochondrial
927 AIF in response to proapoptotic stimuli depends on processing at the intermembrane
928 space. EMBO J. 2005;24(7):1375-86.

929 61. Costello JL, Castro IG, Camoes F, Schrader TA, McNeall D, Yang J, et al. Predicting
930 the targeting of tail-anchored proteins to subcellular compartments in mammalian cells. J
931 Cell Sci. 2017;130(9):1675-87.

932 62. Huang X, Zhou X, Hu X, Joshi AS, Guo X, Zhu Y, et al. Sequences flanking the
933 transmembrane segments facilitate mitochondrial localization and membrane fusion by
934 mitofusin. Proc Natl Acad Sci U S A. 2017;114(46):E9863-E72.

935 63. Jumper J, Evans R, Pritzel A, Green T, Figurnov M, Ronneberger O, et al. Highly
936 accurate protein structure prediction with AlphaFold. Nature. 2021;596(7873):583-9.

937 64. Gonzalvez F, Gottlieb E. Cardiolipin: setting the beat of apoptosis. Apoptosis.
938 2007;12(5):877-85.

939 65. Ardail D, Privat JP, Egret-Charlier M, Levrat C, Lerme F, Louisot P. Mitochondrial
940 contact sites. Lipid composition and dynamics. J Biol Chem. 1990;265(31):18797-802.

941 66. Tamura Y, Endo T, Iijima M, Sesaki H. Ups1p and Ups2p antagonistically regulate
942 cardiolipin metabolism in mitochondria. J Cell Biol. 2009;185(6):1029-45.

943 67. Osman C, Haag M, Potting C, Rodenfels J, Dip PV, Wieland FT, et al. The genetic
944 interactome of prohibitins: coordinated control of cardiolipin and
945 phosphatidylethanolamine by conserved regulators in mitochondria. J Cell Biol.
946 2009;184(4):583-96.

947 68. Kuroda T, Tani M, Moriguchi A, Tokunaga S, Higuchi T, Kitada S, et al. FMP30 is
948 required for the maintenance of a normal cardiolipin level and mitochondrial morphology
949 in the absence of mitochondrial phosphatidylethanolamine synthesis. Mol Microbiol.
950 2011;80(1):248-65.

951 69. van den Brink-van der Laan E, Killian JA, de Kruijff B. Nonbilayer lipids affect
952 peripheral and integral membrane proteins via changes in the lateral pressure profile.
953 Biochim Biophys Acta. 2004;1666(1-2):275-88.

954 70. Joshi AS, Thompson MN, Fei N, Huttemann M, Greenberg ML. Cardiolipin and
955 mitochondrial phosphatidylethanolamine have overlapping functions in mitochondrial
956 fusion in Saccharomyces cerevisiae. J Biol Chem. 2012;287(21):17589-97.

957 71. Signorell A, Rauch M, Jelk J, Ferguson MA, Butikofer P. Phosphatidylethanolamine
958 in Trypanosoma brucei is organized in two separate pools and is synthesized exclusively
959 by the Kennedy pathway. J Biol Chem. 2008;283(35):23636-44.

960 72. Guler JL, Kriegova E, Smith TK, Lukes J, Englund PT. Mitochondrial fatty acid
961 synthesis is required for normal mitochondrial morphology and function in Trypanosoma
962 brucei. Mol Microbiol. 2008;67(5):1125-42.

963 73. Fridberg A, Olson CL, Nakayasu ES, Tyler KM, Almeida IC, Engman DM.
964 Sphingolipid synthesis is necessary for kinetoplast segregation and cytokinesis in
965 Trypanosoma brucei. J Cell Sci. 2008;121(Pt 4):522-35.

966 74. Signorell A, Gluenz E, Rettig J, Schneider A, Shaw MK, Gull K, et al. Perturbation
967 of phosphatidylethanolamine synthesis affects mitochondrial morphology and cell-cycle
968 progression in procyclic-form Trypanosoma brucei. Mol Microbiol. 2009;72(4):1068-79.

969 75. Hirumi H, Hirumi K. Continuous cultivation of Trypanosoma brucei blood stream
970 forms in a medium containing a low concentration of serum protein without feeder cell
971 layers. J Parasitol. 1989;75(6):985-9.

972 76. Wirtz E, Leal S, Ochatt C, Cross GA. A tightly regulated inducible expression
973 system for conditional gene knock-outs and dominant-negative genetics in Trypanosoma
974 brucei. Mol Biochem Parasitol. 1999;99(1):89-101.

975 77. Biebinger S, Wirtz LE, Lorenz P, Clayton C. Vectors for inducible expression of
976 toxic gene products in bloodstream and procyclic Trypanosoma brucei. Mol Biochem
977 Parasitol. 1997;85(1):99-112.

978 78. Ling MM, Robinson BH. Approaches to DNA mutagenesis: an overview. Anal
979 Biochem. 1997;254(2):157-78.

980 79. Wickstead B, Ersfeld K, Gull K. Targeting of a tetracycline-inducible expression
981 system to the transcriptionally silent minichromosomes of Trypanosoma brucei. Mol
982 Biochem Parasitol. 2002;125(1-2):211-6.

983 80. Blancard C, Salin B. Plunge Freezing: A Tool for the Ultrastructural and
984 Immunolocalization Studies of Suspension Cells in Transmission Electron Microscopy. J
985 Vis Exp. 2017(123).

986 81. Jones DT. Protein secondary structure prediction based on position-specific scoring
987 matrices. J Mol Biol. 1999;292(2):195-202.

988 82. Claros MG, Vincens P. Computational method to predict mitochondrially imported
989 proteins and their targeting sequences. Eur J Biochem. 1996;241(3):779-86.

990 83. Hannaert V, Albert MA, Rigden DJ, da Silva Giotto MT, Thiemann O, Garratt RC,
991 Van Roy J, Opperdoes FR, Michels PAM. Kinetic characterization, structure modelling
992 studies and crystallization of Trypanosoma brucei enolase. Eur J Biochem.
993 2003;270:3205-13.
994

995 ***Supplemental material***

996 Figure S1 shows alignment between human and trypanosome mitochondrial dynamin-
997 related proteins.

998 Figure S2 shows alignment of various kineoplastids DBF proteins.

999 Figure S3 shows alignment between *Tb*DBF and various eukaryotes and prokaryotes.

1000 Figure S4 shows growth curves of parental, over-expressing and mutant cells.

1001 Figure S5 shows the inactivation of *Tb*DBF expression by CRISPR/Cas9 system.

1002 Figure S6 shows the down-regulation of *Tb*DBF expression by RNAi.

1003 Figure S7 shows results of the ImageJ plugin on rhodamine-stained cells.

1004 Figure S8 shows the level of overexpression of different *Tb*DBF variants.

1005 Figure S9 shows mitochondrial localization of *Tb*DBF by EM.

1006 Figure S10 shows similar localization of $GFP_{::TM}$ and ^{oe}*Tb*DBFΔMTS.

1007 Figure S11 shows carbon, energy and nitrogen sources used in cells overexpressing
1008 *Tb*DBF.

1009 Table S1 shows results from BLASTp analysis of several identified organisms.

1010 Table S2 shows all the primers and guide RNA used in this study.

1011 Table S3 shows all the antibodies used in this study.

1012 Materials and Methods: MMS1 described the ImageJ macro.

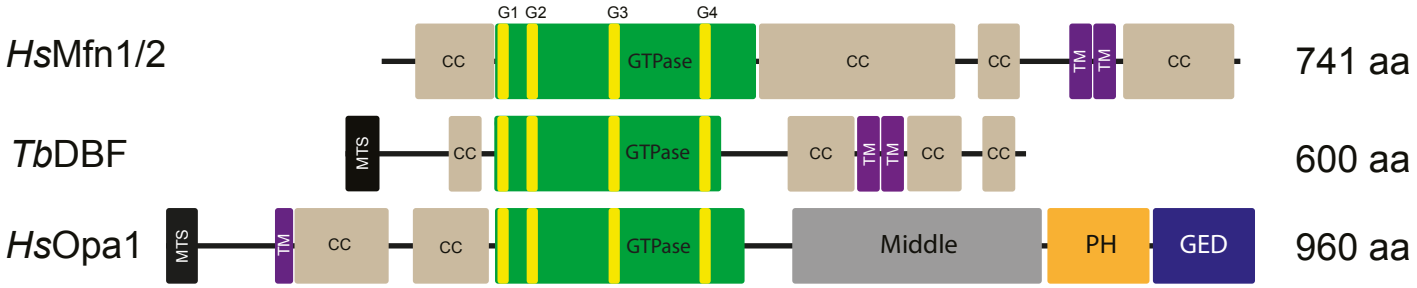

Figure 1 - Structure comparison between mitochondrial dynamin-related proteins (DRPs): Human mitofusin 1 or 2 (*Hs*Mfn1/2), *T. brucei Tb*DBF, and human Opa1 (*Hs*Opa1). MTS, predicted mitochondrial targeting sequence; CC, coiled-coil region; green box, GTPase domain with the four GTP-binding motifs in yellow; TM, transmembrane span; Middle, dynamin middle domain; PH, pleckstrin homology domain; GED, GTPase effector domain. Structure predictions were performed using PSIPRED (Jones, 1999). More details and sequences alignment are shown in Figure S1.

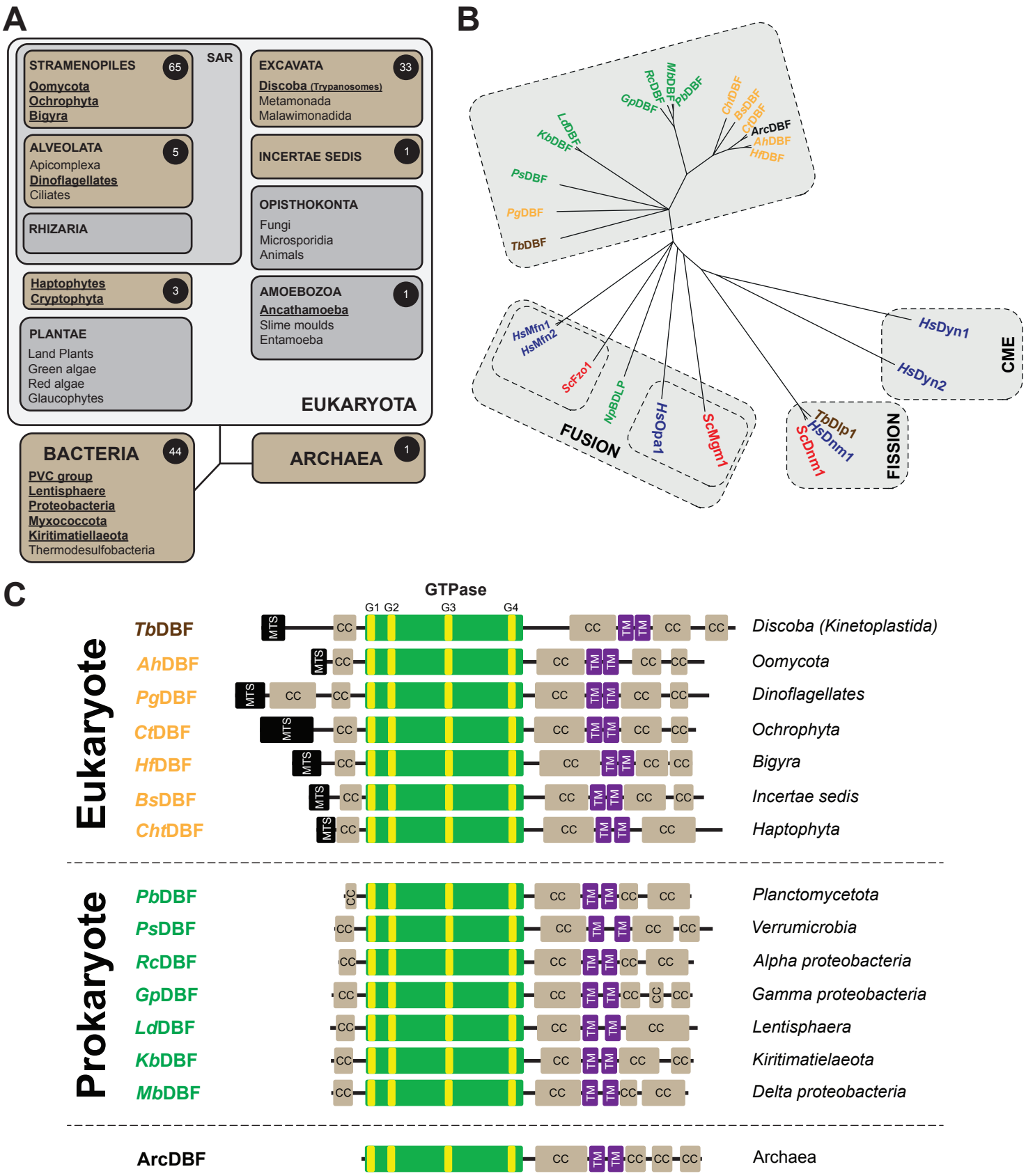

Figure 2 – Homologous sequences to *Tb*DBF, phylogenetic analysis and domain organization of the proteins. (A) Schematic view of the results of the database analysis. The black circles indicate the number of different organisms identified. Bold and underlined characters indicate taxon where homologous sequences were identified. **(B)** Phylogeny of the homologous *Tb*DBF sequences. Trypanosome sequences are highlighted in brown, mammals in blue, yeast in red, other eukaryotes in orange, prokaryote in green and Archaea in black. Mammal, yeast and trypanosome mitochondrial fission and fusion factors were also included as well as the mammals Clathrin-mediated endocytosis dynamins (CME, *Hs*Dyn1 and *Hs*Dyn2). Phylogeny analysis was performed using Geneious software with default parameters (unrooted and scaled). **(C)** Domain organization of several identified proteins from various organisms. MTS, predicted mitochondrial targeting sequence; CC, coiled-coil region; green box, GTPase domain with the four GTP-binding motifs in yellow; TM, transmembrane span; Structure predictions were performed using PSIPRED. More details and sequences alignment are shown in Figure S3. *Tb*DBF, *Trypanosoma brucei* DBF (ID: Tb927.7.2410); *Ah*DBF, *Achlya hypogyna* (ID: OQR970001); *Pg*DBF, *Polarella glacialis* (ID: CAE8737761.1); *Ct*DBF, *Chaetoceros tenuissimus* (ID: GFH50037.1); *Hf*DBF, *Hondaea fermentalgiana* (ID: GBG23909.1); *Bs*DBF, *Bactrachochytrium salamandrivorans* (ID: KAH9255760.1); *Cht*DBF, *Chrysochromulina tobinii* (ID: KOO35358.1); *Pb*DBF, *Planctomycetaceae bacterium* (ID: MBV8881356.1); *Ps*DBF, *Pedosphaera sp.* (ID: MCH2381658.1); *Rc*DBF, *Rubrimonas cliftonensis* (ID: WP_093253540.1); *Gp*DBF, *Gammaproteobacteria bacterium* (ID: RTZ59088.1); *Ld*DBF, *Lentisphaerae bacterium* (ID: NLB69313.1); *Kb*DBF, *Kiritimatiellae bacterium* (MBO7223041.1); *Mb*DBF, *Myxococcota bacterium* (MBU0550280.1). *Arc*DBF, *Archaeon* (ID: RYH26728.1); *Tb*Dlp1, *Trypanosoma brucei* Dlp1 (ID: Tb927.3.4720); *Hs*Dnm1, *Homo sapiens* Dnm1 (ID: AAH50279); *Sc*Dnm1, *Saccharomyces cerevisiae* Dnm1 (ID: AJV55509); *Hs*Dyn1 and *Hs*Dyn2, *homo sapiens* Clathrin-mediated endocytosis dynamins 1 and 2 (ID: KAI2554107.1 and ID: NP_001005360 respectively); *Hs*Opa1, *Homo sapiens* Opa1 (ID: NP_056375); *Sc*Mgm1, *Saccharomyces cerevisiae* Mgm1 (ID: NP_014854); *Np*BDLP, *Nostoc punctiforme* (ID: WP_012412711); *Hs*Mfn1 and *Hs*Mfn2, *Homo sapiens* Mfn1 and 2 (ID: NP_284941 and ID: NP_001121132 respectively); *Sc*Fzo1, *Saccharomyces cerevisiae* Fzo1 (ID: NP_009738).

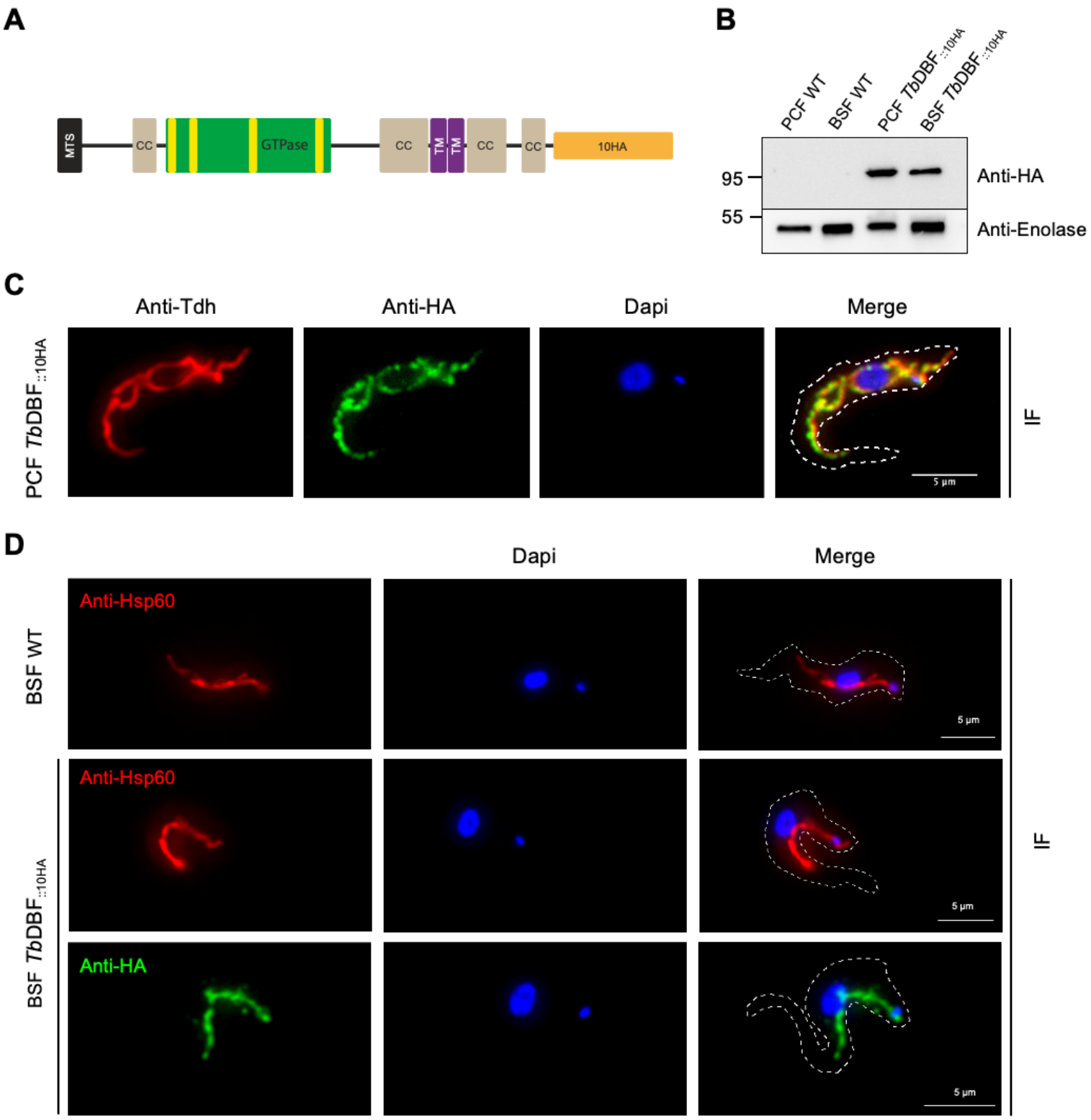

Figure 3 - Subcellular localization of *Tb*DBF. (A) Schematic representation of *Tb*DBF endogenously tagged its at C-terminus extremity with 10xHA. Only one of the two alleles is tagged. **(B)** Western blotting of whole-cell extracts ($5x10^6$ cells) of *T. brucei* PCF or BSF wild-type cells and PCF or BSF expressing *Tb*DBF$_{::10HA}$ cells revealed with an anti-HA antibody. It should be noted that Enolase used as a loading control is about 3 to 4 times more expressed in BSF than PCF according to Hannaert *et al.* (82). **(C)** Subcellular localization of *Tb*DBF$_{::10HA}$ in PCF. Colocalization of *Tb*DBF$_{::10HA}$ (anti-HA antibody) with matrix mitochondrial threonine dehydrogenase (Anti-Tdh antibody) analyzed by standard immunofluorescence. **(D)** Subcellular localization of *Tb*DBF$_{::10HA}$ in BSF. Matrix mitochondrial Heat shock protein 60 (Anti-Hsp60 antibody) was used to labelled the mitochondrial compartment in wild-type and *Tb*DBF$_{::10HA}$ cells.

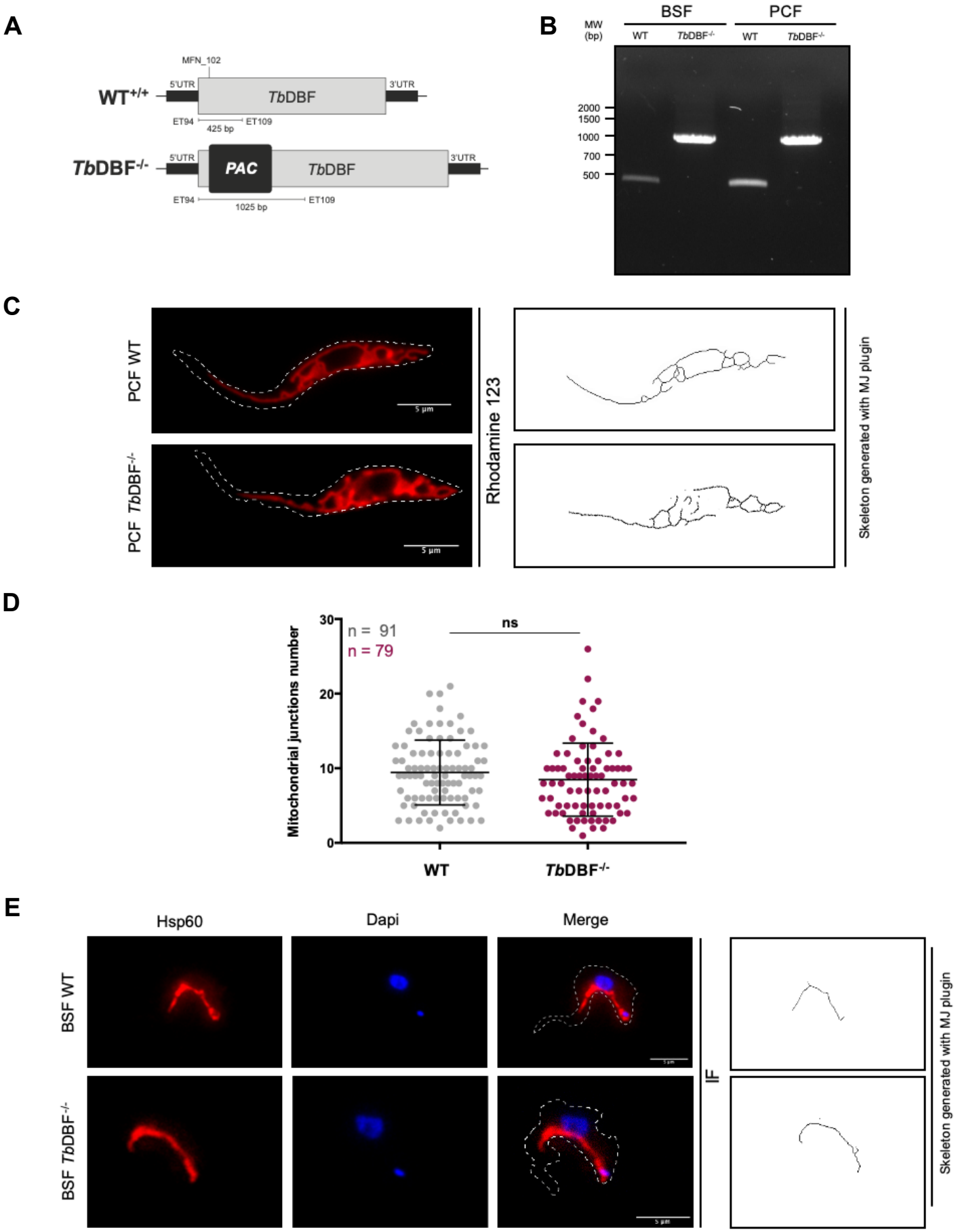

Figure 4 - Inactivation of the *Tb*DBF gene. (A) Schematic representation of *Tb*DBF inactivation by insertion of the puromycine resistant marker (PAC). **(B)** PCR confirmation of *Tb*DBF gene inactivation on both alleles in BSF and PCF. **(C)** The mitochondrial shape of living WT and *Tb*DBF$^{-/-}$ PCF cells (right panel) was designed by an ImageJ macro (MJ, Mitochondrial Junctions) from rhodamine 123 staining (left panel). **(D)** Corresponding mitochondrial junctions quantification. **(E)** Antibody directed against Hsp60 was used to label and visualized mitochondrial shape in BSF cells. Top panel : BSF WT cell; bottom panel : BSF *Tb*DBF$^{-/-}$ cell. Statistic : t test - Confidence interval 95% - P-value style : 0.1234 (ns); 0.0332 (*); 0.0021 (**); 0.0002 (***); <0.0001 (****).

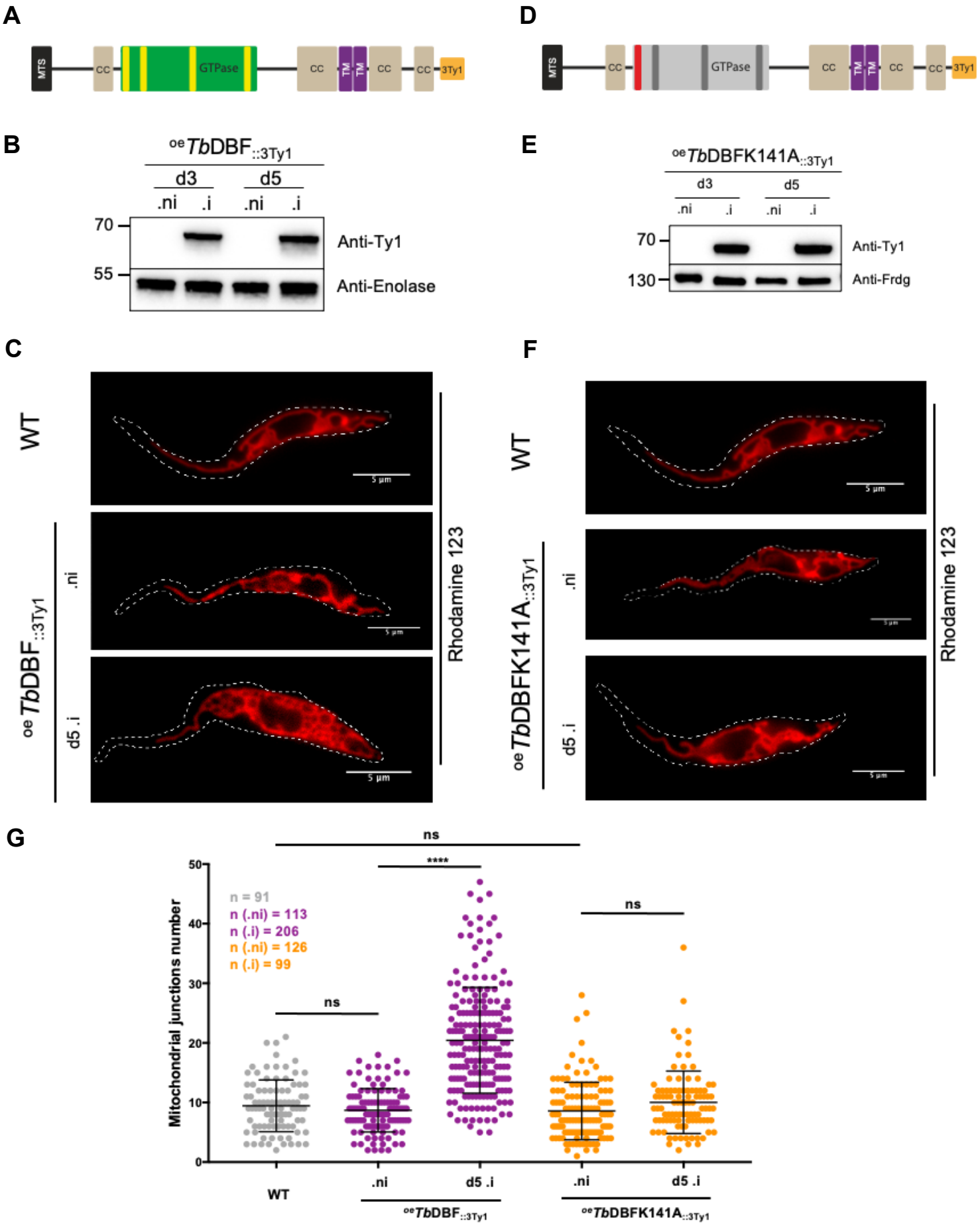

Figure 5 - Overexpression of *Tb*DBF and GTPase mutant. (A) Schematic representation of overexpressing *Tb*DBF protein tagged with 3Ty1 peptide at C-terminus of the protein (^{oe}*Tb*DBF$_{::3Ty1}$). **(B)** Western blotting of whole-cell extracts of *T. brucei* PCF overexpressing *Tb*DBF$_{::3Ty1}$ cells. Non-induced (ni) and induced (i) cells after 3 to 5 days (d3 and d5) were revealed with an anti-Ty1 antibody. Antibody directed against Enolase protein (Eno) was used as loading control. **(C)** Mitochondrial structure analysis using rhodamine 123 staining on living cells; mitochondrial structure of PCF WT and PCF ^{oe}*Tb*DBF$_{::3Ty1}$ cells before (ni) and 5 days after (i) tetracycline induction. **(D)** Schematic representation of overexpressing *Tb*DBFK141A$_{::3Ty1}$ mutant protein tagged with 3Ty1 peptide at the C-terminus of the protein (^{oe}*Tb*DBFK141A$_{::3Ty1}$). **(E)** Western blotting of whole-cell extracts of *T. brucei* PCF overexpressing *Tb*DBFK141A$_{::3Ty1}$ cells; (ni) non-induced and (i) induced cells for 3 or 5 days (d3 and d5). Antibody directed against glycosomal Fumarate reductase protein (Frdg) was used as loading control. **(F)** Mitochondrial structure analysis using rhodamine 123 staining on living cells; mitochondrial structure of PCF WT and PCF ^{oe}*Tb*DBFK141A$_{::3Ty1}$ cells before (ni) and 5 days after (i) tetracycline induction. **(G)** quantification of mitochondrial junctions number using Rhodamine 123 microscopy images. Mitochondrial junctions number: WT, 9.4 ± 4.3; .ni ^{oe}*Tb*DBF$_{::3Ty1}$ 8.7 ± 3.6; .i ^{oe}*Tb*DBF$_{::3Ty1}$ 20.4 ± 8.9; .ni ^{oe}*Tb*DBFK141A$_{::3Ty1}$ 8.6 ± 4.8 and .i ^{oe}*Tb*DBFK141A$_{::3Ty1}$ 10 ± 5.2. Statistic : t test - Confidence interval 95% - P-value style : 0.1234 (ns); 0.0332 (*); 0.0021 (**); 0.0002 (***); <0.0001 (****).

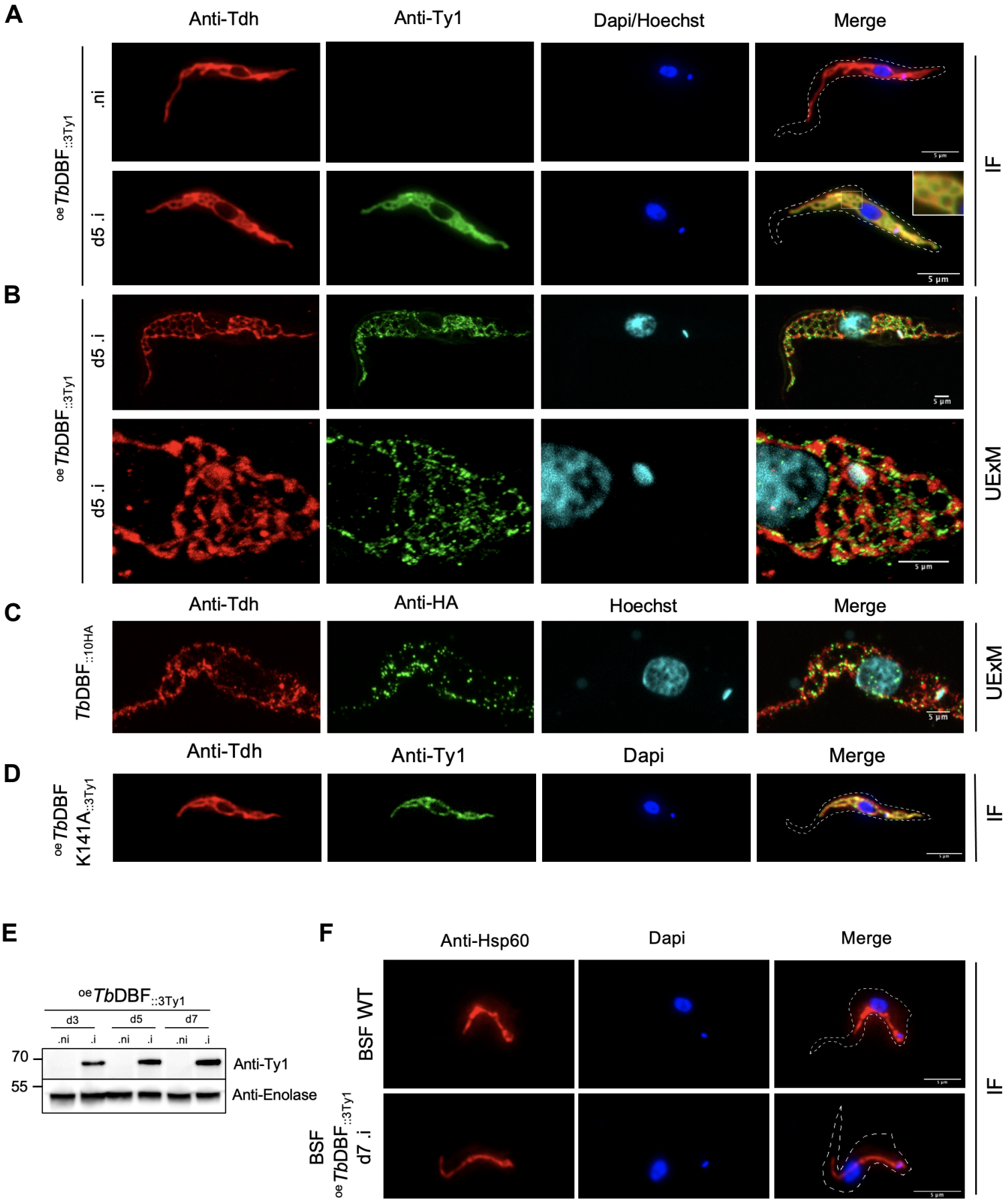

Figure 6 - Overexpression of *Tb*DBF and GTPase mutant. Subcellular localization of ^{oe}*Tb*DBF$_{::3Ty1}$ in PCF by immunofluorescence and Ultra Expansion Microscopy (UExM); Colocalization of ^{oe}*Tb*DBF$_{::3Ty1}$ (anti-Ty1 antibody) with matrix mitochondrial Threonine dehydrogenase (Anti-Tdh antibody) was analyzed by standard immunofluorescence **(A)** and by UExM with an expansion factor of ~4.4 **(B)**, after 5 days induction (d5.i). **(C)** Subcellular localization of *Tb*DBF$_{::10HA}$ in PCF analyzed by UExM. **(D)** Subcellular localization of ^{oe}*Tb*DBFK141A$_{::3Ty1}$ in PCF analyzed by standard immunofluorescence. **(E)** Western blotting of whole-cell extracts of *T. brucei* BSF overexpressing *Tb*DBF$_{::3Ty1}$ cells. Non-induced (ni) and induced (i) cells after 3 to 7 days (d3, d5 and d7) were revealed with an anti-Ty1 antibody. Antibody directed against Enolase protein (Eno) was used as loading control. **(F)** Subcellular localization of ^{oe}*Tb*DBF$_{::3Ty1}$ in BSF by immunofluorescence. Antibody directed against Hsp60 was used to label and visualized mitochondrial shape in wild type and *Tb*DBF$_{::3Ty1}$ overexpressing cells.

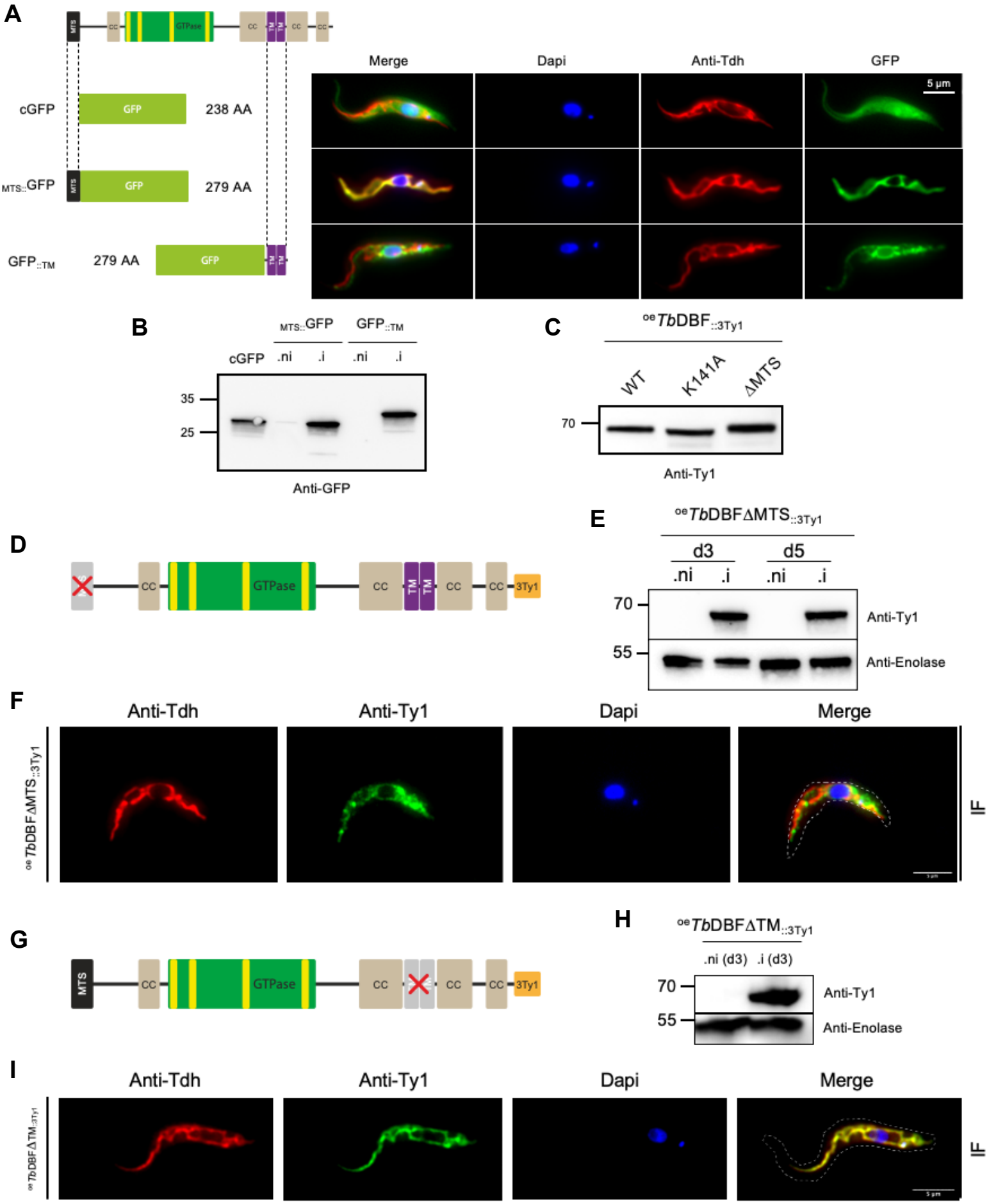

Figure 7 - Role of *Tb*DBF domains. (A) Localization of the GFP according to the different tags fused. Colocalization by standard immunofluorescence of GFP with matrix mitochondrial Threonine dehydrogenase (Anti-Tdh antibody) after 5 days induction. MTS, mitochondrial targeting signal; TM, transmembrane domains. **(B)** Western-blot analysis of GFP expression. cGFP, constitutive and cytosolic GFP. Non-induced (ni) and induced (i) cells after 5 days. **(C)** *Tb*DBF size analysis by western-blot using anti-Ty1 antibody. **(D)** Schematic representation of N-terminus truncated *Tb*DBF protein (first 41 amino acids) tagged with 3Ty1 peptide at the C-terminus of the protein (^{oe}*Tb*DBFΔMTS$_{::3Ty1}$). **(E)** Western blotting of whole-cell extracts of *T. brucei* PCF overexpressing *Tb*DBFΔMTS$_{::3Ty1}$ cells; (ni) non-induced and (i) induced cells for 3 or 5 days (d3 and d5). **(F)** Subcellular localization of ^{oe}*Tb*DBFΔMTS$_{::3Ty1}$ in PCF after 5 days induction. Colocalization of ^{oe}*Tb*DBFΔMTS$_{::3Ty1}$ (anti-Ty1 antibody) with matrix mitochondrial Threonine dehydrogenase (Anti-Tdh antibody) analyzed by standard immunofluorescence. **(G)** Schematic representation of truncated transmembrane domains of *Tb*DBF protein (45 amino acids) tagged with 3Ty1 peptide at the C-terminus of the protein (^{oe}*Tb*DBFΔTM$_{::3Ty1}$). **(H)** Western blotting of whole-cell extracts of *T. brucei* PCF overexpressing *Tb*DBFΔTM$_{::3Ty1}$ cells; (ni) non-induced and (i) induced cells for 3 days. **(I)** Subcellular localization of ^{oe}*Tb*DBFΔTM$_{::3Ty1}$ in PCF after 5 days induction, analyzed by standard immunofluorescence.

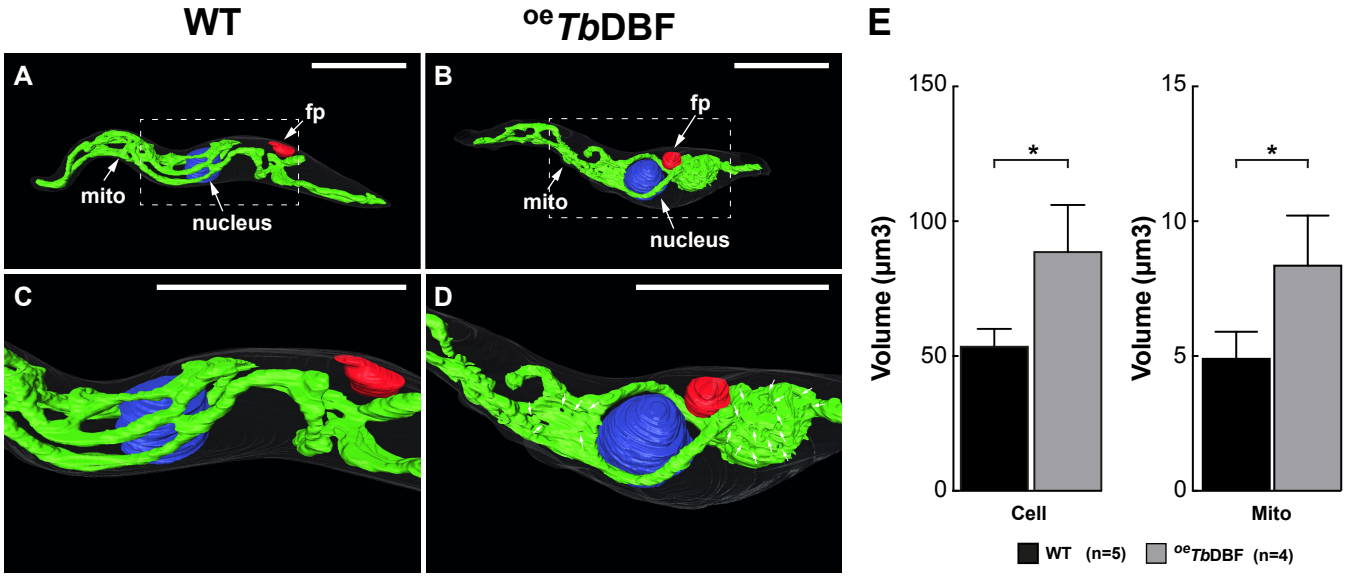

Figure 8 - Surface rendering of segmented PCF and determination of cell, nucleus and mitochondrion volumes using SBF-SEM. (A/B) Surface rendering of a segmented PCF (WT and *oeTb*DBF) showing the cell body (transparency), nucleus (blue), mitochondrion (green), and flagellar pocket (red). **(C/D)** Magnified view of the region boxed in A and B. Small arrows indicate mitochondria-free spaces in the mitochondrial network. The scale bar represents 5 µm. **(E)** Changes in the mean volumes of the cell and mitochondria. The n values are indicated on the right side of the legend. Volume in µm3, cell: WT 53.4±6.6, *oeTb*DBF 88.6±17.5; mitochondrion: WT 4.9±1, *oeTb*DBF 8.3±1.9. Statistic : t test - Confidence interval 95% - P-value style : 0.1234 (ns); 0.0332 (*); 0.0021 (**); 0.0002 (***); <0.0001 (****).

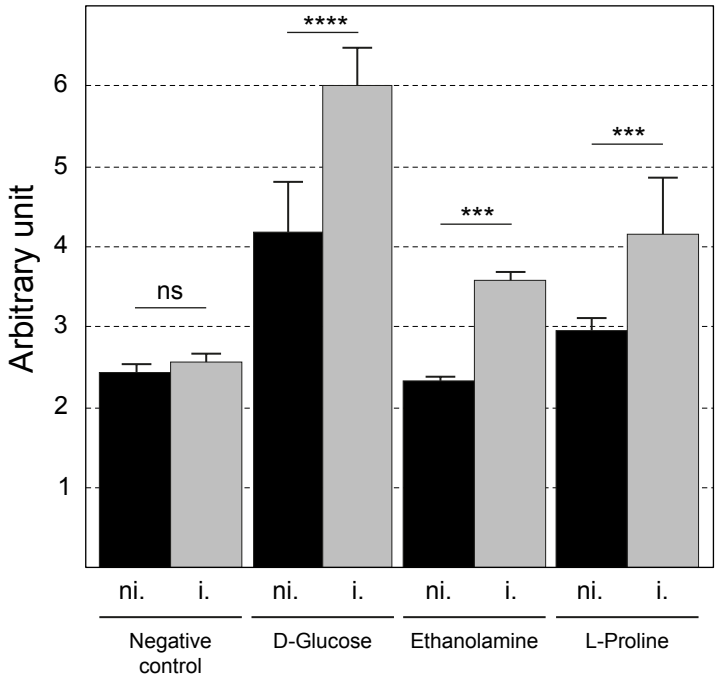

Figure 9 - Carbon sources used in cells overexpressing ^{oe}*Tb*DBF$_{::3Ty1}$. The metabolic pathway activities are assayed using a colorimetric reagent that measures redox production when a cell oxidizes a substrate (Biolog Phenotype MicroArrays™). Non-induced (black) and induced (grey) cells were incubated for 18 hours at 27°C with various substrates and redox production was measured by an endpoint absorbance at 590 nm. Only the 3 carbon sources showing significant variation are presented among the 119 molecules used. All the molecules (carbon and nitrogen sources) are show in Figure S11. The negative control corresponds to an absence of carbon sources. Statistic : Two way ANOVA - Confidence interval 95% - P-value style : 0.1234 (ns); 0.0332 (*); 0.0021 (**); 0.0002 (***); <0.0001 (****), n=3.

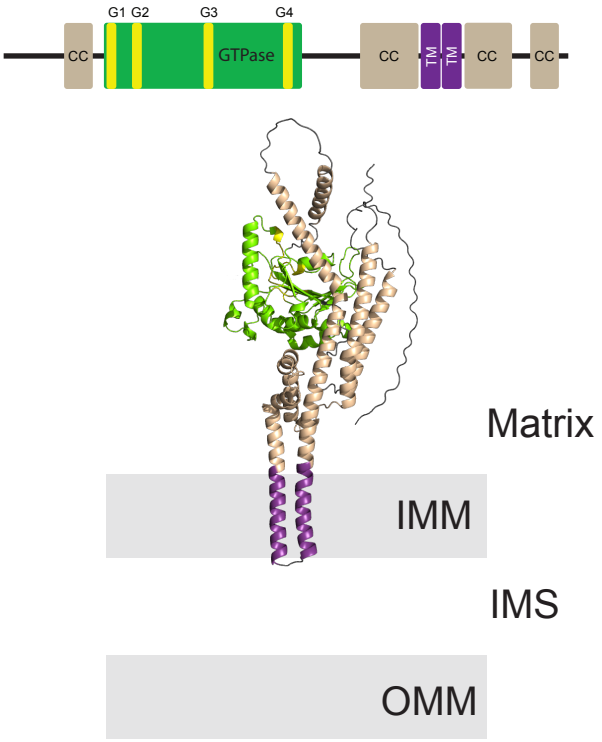

Figure 10 – Proposed submitochondrial localization and membrane topology of *Tb*DBF. Predicted structure of *Tb*DBF, from AlphaFold protein structure database. *Tb*DBF was embedded in mitochondrial inner membrane (IMM). The color coding correspond to the predicted secondary structure depicted on the top of the figure. The N-terminus MTS was not displayed as it is cleaved. The AlphaFold model score of *Tb*DBF is between confident to very high for most of the structured regions (https://alpha-fold.ebi.ac.uk/entry/Q57XN3).